

Machine-assisted discovery of integrable symplectic mappings

T. Zolkin^{✉*}

Fermilab, PO Box 500, Batavia, Illinois 60510-5011, USA

Y. Kharkov

Joint Center for Quantum Information and Computer Science, NIST/University of Maryland, College Park, Maryland 20742, USA
and Joint Quantum Institute, NIST/University of Maryland, College Park, Maryland 20742, USA

S. Nagaitsev^{✉†}

Jefferson Lab, Newport News, Virginia 23606, USA

and Old Dominion University, Norfolk, Virginia 23529, USA



(Received 22 March 2022; revised 2 February 2023; accepted 8 September 2023; published 13 December 2023)

We present a new automated method for finding integrable symplectic maps of the plane. These dynamical systems possess a hidden symmetry associated with an existence of conserved quantities, i.e., integrals of motion. The core idea of the algorithm is based on the knowledge that the evolution of an integrable system in the phase space is restricted to a lower-dimensional submanifold. Limiting ourselves to polygon invariants of motion, we analyze the shape of individual trajectories thus successfully distinguishing integrable motion from chaotic cases. For example, our method rediscovers some of the famous McMillan-Suris integrable mappings and ultradiscrete Painlevé equations. In total, over 100 new integrable families are presented and analyzed; some of them are isolated in the space of parameters, and some of them are families with one parameter (or the ratio of parameters) being continuous or discrete. At the end of the paper, we suggest how newly discovered maps are related to a general 2D symplectic map via an introduction of discrete perturbation theory and propose a method on how to construct smooth near-integrable dynamical systems based on mappings with polygon invariants.

DOI: [10.1103/PhysRevResearch.5.043241](https://doi.org/10.1103/PhysRevResearch.5.043241)

I. INTRODUCTION

Integrable systems play a fundamental role in mathematics and physics, particularly in dynamical system theory, due to well-understood dynamics. Integrability is generally defined as the existence of a sufficient number of functionally independent conserved quantities (integrals of motion) in involution, which are related to intricate hidden symmetries. Hence, in many cases the construction of integrable systems often requires some special fine-tuning. This makes them very difficult to discover. Although integrable models occupy measure-zero in the space of parameters, they play a crucial role in the theory of dynamical systems. In fact, they shed light on the properties of more generic near-integrable cases via Kolmogorov-Arnold-Moser (KAM) theorem and various perturbation theories.

While the concept of integrability is most often discussed in the context of continuous-time systems, it also arises in discrete-time maps [1]. Mappings are of profound importance

in the field of dynamical system theory exhibiting a broad range of behaviours including dynamical chaos, bifurcations, strange attractors, and integrability [2]. On the one hand, they can be used as an approximation of a continuous flow (since in many cases the discretized form can be easier to study) or, on the other hand, as a reduction to a lower-dimensional manifold, e.g., considering Poincaré cross-sections.

A particularly valuable class of discrete dynamical systems are symplectic maps, associated with Hamiltonian flows, e.g., a 2D area-preserving map is equivalent to a Hamiltonian system with 1 degree of freedom and a potential energy that is periodic in time. Symplectic maps arise as effective models in a wide range of domains, such as celestial mechanics, plasma hydrodynamics, fluid flows, and particle accelerators [3].

Although area-preserving maps of the plane have been studied for decades, only a handful of integrable cases have been discovered. The existence of integrals of motion restricts phase space dynamics to a set of nested tori. Any discovery of novel integrable maps is highly nontrivial and historically has been accomplished by scientists making inspired guesses and applying relevant analytical tools. In many cases, even the proof of the integrability of a specific mapping is quite challenging.

An automated search for integrable systems remains a nontrivial task: Only a few successful examples exist to date where machine-assisted searches resulted in new discoveries in nonlinear dynamics. For example, computer-assisted searches combined with high precision simulations

*zolkin@fnal.gov

†nsergei@jlab.org

found new families of periodic orbits in a gravitational three-body problem [4–6]. Recent works utilized machine-learning methods to discover integrals of motion of classical dynamical systems from phase space trajectories, e.g., Refs. [7–10]. These examples employed a computer-assisted search to either discover new families of trajectories or to rediscover previously known invariants of motion in integrable systems. In contrast, our algorithm has found previously unknown integrable symplectic maps, advancing the theory of integrable systems.

In this paper, we propose and describe this new algorithm for discovering area-preserving integrable maps of the plane. While scanning over a large space of potential candidate maps, our algorithm traces out individual orbits and subsequently analyzes shapes of invariant manifolds. We restricted our search to the family of mappings which possess integrals of motion with a polygon geometry, thus constraining our search to piecewise linear transformations of the plane. Piecewise linear mappings could be regarded as the simplest possible dynamical systems with rich nonlinear dynamics, which makes them an attractive model to study. They could be viewed as fundamental building blocks of generic integrable symplectic maps. An arbitrary smooth 2D symplectic map could be approximated as an n -piece piecewise linear map, but only in the uniform sense, see Sec. VIB. By applying a machine-assisted search, we found over a hundred new integrable mappings; some of them are isolated in the space of parameters, and some of them are families with one parameter (or the ratio of parameters) being continuous ($\in \mathbb{R}^{(+)}$) or discrete ($\in \mathbb{Z}^{(+)}$).

The structure of this article is as follows. In Sec. II we provide a historical overview of integrability of symplectic mappings of the plane. In Secs. III and IV we review linear integrable mappings produced by one- and two-piecewise linear force functions. At the end of Sec. IV we introduce new nonlinear integrable maps with polygon invariants, and in Sec. V we propose an algorithm for the machine-assisted discovery of integrable systems with more complicated force functions. Section VIB presents the main results of our search, and finally, in Sec. VI we discuss some practical applications of mappings with polygon invariants. In Appendix A, we provide the connection between systems discovered in this article and some of the ultradiscrete Painlevé equations [11,12]. The pseudocode for the search algorithm and list of integrable cases are placed at the end of the article in Appendices B and C.

II. 2D SYMPLECTIC MAPPINGS AND INTEGRABILITY: HISTORICAL OVERVIEW

The most general form of an autonomous 2D mapping of the plane, $\mathcal{M} : \mathbb{R}^2 \rightarrow \mathbb{R}^2$, can be written as

$$\begin{aligned} q' &= F(q, p), \\ p' &= G(q, p), \end{aligned}$$

where $'$ denotes an application of the map, and F and G are functions of both variables. If the Jacobian of a 2D map, $J \equiv \partial_q F \partial_p G - \partial_p F \partial_q G$, is equal to unity, then the map is *area-preserving* and thus also *symplectic* (for higher

dimensional mappings, area-preservation is necessary but not sufficient for a map to be symplectic). A map is called *integrable* in a Liouville sense [13] if there exists a real-valued continuous function $\mathcal{K}(p, q)$ called an *integral of motion* (or *invariant*), for which the level sets $\mathcal{K}(p, q) = \text{const}$ are curves (or sets of points) and

$$\forall (q, p) \in \mathbb{R}^2 : \quad \mathcal{K}(p', q') = \mathcal{K}(p, q).$$

The first nonlinear symplectic integrable map of the plane was discovered by E. McMillan [14] when he studied a specific form of the map

$$\begin{aligned} q' &= p, \\ p' &= -q + f(p), \end{aligned} \tag{1}$$

where $f(p)$ will be called the *force function*. We will refer to this mapping as the *McMillan-Hénon form* or the MH form for short (please do not confuse with *McMillan integrable map* [14], which is a special case when $f(p)$ is given by a ratio of two quadratic polynomials).

At first, the choice of the MH form (1) might look very restrictive and unmotivated. McMillan's original idea was based on its simplicity and clear symmetries (which will be described in detail below), which still allowed some degree of freedom in modifying the dynamics by varying $f(p)$. As it was demonstrated later by Turaev [15], almost every symplectic map of the plane (and even 2nD symplectic map) can be approximated by iterations of MH maps. In this article, we will restrict our consideration to this form; however, our results can be easily generalized to different representations of the map.

Below we summarize several important results regarding the integrability of mappings in a McMillan-Hénon form:

(1) First, the family of integrable mappings of the plane in the MH form were discovered by McMillan [14] for a biquadratic invariant in the form

$$\begin{aligned} (I) : \quad \mathcal{K}(p, q) = & A p^2 q^2 + B (p^2 q + p q^2) \\ & + \Gamma (p^2 + q^2) + \Delta p q + E (p + q), \end{aligned}$$

corresponding to the force function

$$f(p) = \frac{B p^2 + \Delta p + E}{A p^2 + B p + \Gamma}$$

and integrable for any values of parameters A, B, Γ, Δ and E [Fig. 1(a)].

(2) Later, Suris [16] studied the integrability of a difference equation in the form

$$x_{n+1} + x_{n-1} = f(x_n),$$

referred to as the *Suris form of the map* (sometimes referred to as the *standard type*). The Suris form of the mapping has a clear physical interpretation, since in the continuous-time limit it takes the form of a 1D Newton equation $\ddot{x} = f(x) - 2x$, where the right hand side plays the role of a mechanical force. Mapping in the Suris form is just another representation of the MH form by setting $q_n = x_n$ and $p_n = x_{n+1}$ (one can think of an analogy between the Lagrangian approach with a single differential equation of the second order, and the Hamiltonian approach with two differential equations of the

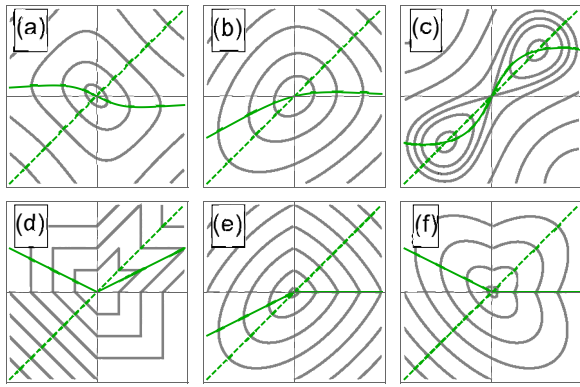


FIG. 1. Invariant level sets, $\mathcal{K}(p, q) = \text{const}$, for integrable mappings in the MH form. McMillan-Suris mappings I–III, respectively, panels (a)–(c), with $A, \Gamma, \Delta, \Lambda_{1,3} = -\Lambda_2 = 1$ and $B, E, \psi, \phi = 0$. Brown-Knuth map (d) along with McMillan beheaded (e) and two-headed (f) ellipses. All mappings are shown for the range $q, p \in [-2, 2]$. The dashed and solid dark green lines show the first and second symmetry lines.

first order, e.g., see Ref. [13]). Suris proved that for analytic force functions $f(p)$ and $\mathcal{K}(p, q)$, the invariant of the integrable mapping can take only one of the following forms: (I) biquadratic function of p and q (McMillan map), (II) biquadratic exponential or (III) trigonometric polynomial:

$$\begin{aligned} \text{(II)} : \mathcal{K}(p, q) = & A e^{\alpha p} e^{\alpha q} + B (e^{\alpha p} + e^{\alpha q}) \\ & + \Gamma (e^{\alpha p} e^{-\alpha q} + e^{-\alpha p} e^{\alpha q}) \\ & + \Delta (e^{-\alpha p} + e^{-\alpha q}) + E e^{-\alpha p} e^{-\alpha q}, \end{aligned}$$

$$\begin{aligned} \text{(III)} : \mathcal{K}(p, q) = & \Lambda_1 (\cos[\omega p - \psi] + \cos[\omega q - \psi]) \\ & + \Lambda_2 \cos[\omega(p + q) - \phi] \\ & + \Lambda_3 \cos[\omega(p - q)]. \end{aligned}$$

Maps (I–III) are integrable for any choice of parameters, see some examples with invariant level sets in Figs. 1(a)–1(c). Results by Suris greatly reduce possible forms of $f(p)$ corresponding to integrable cases.

(3) In 1983, Morton Brown proposed an interesting problem in the section “Advanced Problems” of Amer. Math. Monthly [17].

6439. Let $\{x_n\}$ be a sequence of real numbers satisfying the relation $x_{n+1} = |x_n| - x_{n-1}$. Prove that $\{x_n\}$ is periodic with period 9.

One can notice that this map is in the Suris form (so it can be written in the MH form as well) with $f(p) = |p|$.

In 1985, the solution by Slifker was published in Ref. [18] with a comment below:

Also solved by the proposer and sixty-one others. The problem turned out to be rather elementary.

Despite its “simplicity,” the map has proven to be interesting for dynamical system theory, combinatorics and topology. 10 years later, in 1993, Brown extended his results to the formal publication [19]. He reconsidered the equation as the homeomorphism of the plane and provided a geometrical proof of periodicity including a description of the polygon

invariant of motion [see Fig. 1(d)]:

$$\begin{aligned} \mathcal{K}(p, q) = & q + |p - |q - |p||| + |q - |p - |q||| \\ & + |q - |p|| + |p - |q| + |q - |p - |q|||. \end{aligned}$$

Knuth, who provided his own combinatorical proof of periodicity, wrote a letter to Brown:

When I saw advanced problem 6439, I couldn't believe that it was “advanced”: a result like that has to be either false or elementary!

But I soon found that it wasn't trivial. There is a simple proof, yet I can't figure out how on earth anybody would discover such a remarkable result. Nor have I discovered any similar recurrence relations having the same property. So in a sense I have no idea how to solve the problem properly. Is there an “insightful” proof, or is the result simply true by chance?

While quite often this map is referred to as Knuth map, we would like to call it *Brown-Knuth map* to acknowledge all contributors.

(4) Finally, in his original article [14], Edwin McMillan suggested another intricate integrable system with a piecewise quadratic invariant and a piecewise linear force function

$$\mathcal{K}(p, q) = \begin{cases} p^2 + a p q + q^2, & p, q \geq 0, \\ p^2 - a p q + q^2, & \text{otherwise,} \end{cases}$$

and

$$f(p) = \begin{cases} a p, & q < 0, \\ 0, & q \geq 0, \end{cases}$$

where $a \in \mathbb{R}$ is an arbitrary coefficient. He referred to the corresponding invariant level sets as *beheaded* and *two-headed ellipses*, see Figs. 1(e) and 1(f). As we will see in Sec. IV A 2, this map as well as the Brown-Knuth map are examples of more general integrable systems with the force function $f(p) = a p + b |p|$ and invariants being a collection of ellipses, hyperbolas and straight lines (segments).

(5) Last, we should mention a special class of finite difference equations, which are integrable (in the sense that they admit a Lax pair representation), known as discrete Painlevé equations. Discrete Painlevé equations are closely related to integrable symplectic maps of the plane. We discuss the connection in Appendix A.

Several properties of MH mappings (1) which will help us understand and interpret further results are:

(1) A map in the MH form is symplectic for any continuous $f(p)$.

(2) The map \mathcal{M} in the MH form is reversible with the inverse

$$\mathcal{M}^{-1} : \begin{cases} q' = -p + f(q), \\ p' = q. \end{cases}$$

(3) For any map with $f(p)$ there is a *twin map* with the mirrored force function $-f(-p)$, so that their dynamics are identical up to a rotation of phase space by an angle of π , $(p, q) \rightarrow -(p, q)$. Thus, we will omit twin maps unless it is necessary.

(4) An MH map can be decomposed into two transformations $\mathcal{M} = \mathcal{F} \circ \text{Rot}(\pi/2)$, where

$$\text{Rot}(\pi/2) : \begin{cases} q' = p, \\ p' = -q, \end{cases} \quad \mathcal{F} : \begin{cases} q' = q, \\ p' = p + f(q), \end{cases}$$

with $\text{Rot}(\theta)$ being a *rotation* (about the origin by an angle θ):

$$\text{Rot}(\theta) : \begin{bmatrix} q' \\ p' \end{bmatrix} = \begin{bmatrix} \cos \theta & \sin \theta \\ -\sin \theta & \cos \theta \end{bmatrix} \begin{bmatrix} q \\ p \end{bmatrix}$$

and \mathcal{F} being a *thin lens* transformation. The name “thin lens” comes from optics and reflects that the transformation is localized so coordinates remain unchanged, $q' = q$, and momentum (or angle in optics) is changed according to location, $\Delta p \equiv p' - p = f(q)$. Both transformations are area-preserving and symplectic. This decomposition is very important and explains the physical nature of the map representing a particle kicked periodically in time with the force $f(q)$. A general model of kicked oscillators includes famous examples of Chirikov map [20,21], Hénon map [22], and many others. In particular, this decomposition is often employed in accelerator physics; a model accelerator with one degree of freedom consisting of a linear optics insert and a thin nonlinear lens (such as sextupole or McMillan integrable lens) can be rewritten in the MH form.

(5) An MH map can be decomposed into the superposition of two transformations $\mathcal{M} = \mathcal{G} \circ \text{Ref}(\pi/4)$, where

$$\text{Ref}(\pi/4) : \begin{cases} q' = p, \\ p' = q, \end{cases} \quad \mathcal{G} : \begin{cases} q' = q, \\ p' = -p + f(q), \end{cases}$$

with $\text{Ref}(\theta)$ being a *reflection* about a line passing through the origin at an angle θ with the q axis

$$\text{Ref}(\theta) : \begin{bmatrix} q' \\ p' \end{bmatrix} = \begin{bmatrix} \cos 2\theta & \sin 2\theta \\ \sin 2\theta & -\cos 2\theta \end{bmatrix} \begin{bmatrix} q \\ p \end{bmatrix}$$

and \mathcal{G} being a special *nonlinear vertical reflection*. Transformation \mathcal{G} leaves the horizontal coordinate invariant, $q' = q$, while a point is reflected vertically with respect to the line $p = f(q)/2$, i.e., equidistant condition

$$p' - f(q)/2 = f(q/2) - p$$

is satisfied.

Both reflections are *anti-area-preserving* (the determinant of Jacobian is equal to -1) and are *involutions*, i.e., a double application of the map is identical to transformation $\text{Ref}^2(\theta) = \mathcal{G}^2 = I_2$. In addition, each reflection has a line of fixed points: $p = q$ for $\text{Ref}(\pi/4)$ (further referred to as the *first symmetry line*) and $p = f(q)/2$ for \mathcal{G} (further referred to as the *second symmetry line*); see Fig. 2.

(6) Fixed points of the map are given by the intersection of the two symmetry lines and always in I or III quadrants:

$$p^* = q^* = f(q)/2.$$

(7) Two-cycles (if any) are given by the intersection of the second symmetry line $p = f(q)/2$ with its inverse $q = f(p)/2$ (so the intersection is always in the II and IV quadrants). Additionally, if $f(p)$ is an odd function, then two-cycles are restricted to antidiagonal $p = -q$.

(8) Finally, the last and most important property we would like to list here: any constant invariant level set of an integrable MH map (either a point, set of points, closed and

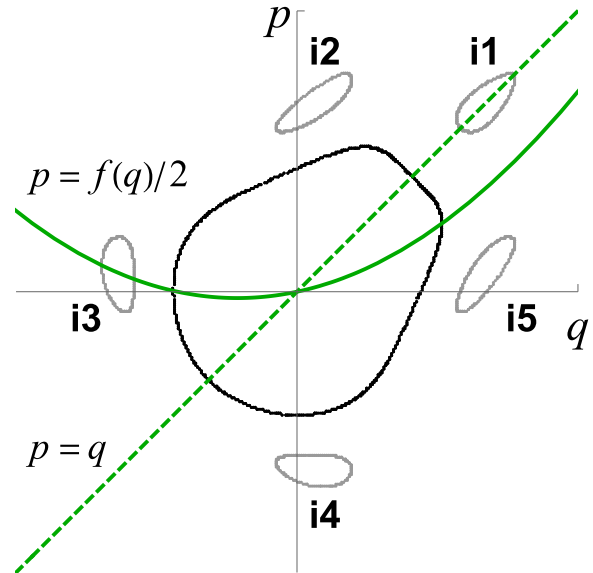


FIG. 2. Two constant level sets $\mathcal{K}(p, q) = \text{const}$ for the chaotic Hénon map, $f(p) = a p + b p^2$. The black curve shows a closed trajectory encompassing the origin and the gray curves show a set of islands (i.e., under iterations, points hop from island to island covering the closed gray curves labeled i1–i5). While the first (reflection) symmetry is quite obvious from the figure, we will focus on the second one. The upper branch of the blue curve, $\Phi(q)$, is vertically equidistant from the lower branch, $\Phi^{-1}(q)$. Island i3 satisfies the second symmetry in the same manner as does the blue curve. Islands i1 and i2 satisfy the symmetry in a sense that they are vertical reflections of islands i5 and i4, respectively (e.g., the lower part of i1 is equidistant from the upper part of i5 and the upper part of i1 is equidistant from the lower part of i5). The dashed and solid green lines are the first and second symmetry lines.

open curves, or even collection of closed curves representing islands) is invariant under both reflections, $\text{Ref}(\pi/4)$ and \mathcal{G} . If $f(p)$ is an odd function, then invariant level sets possess additional symmetry $\mathcal{K}(p, q) = \mathcal{K}(-p, -q)$, meaning that the map coincides with its twin.

Invariance under these transformations results in two geometrical consequences, first noticed in relation to integrability by McMillan [14]. First, invariant level sets are symmetric with respect to transformation $\text{Ref}(\pi/4)$:

$$\mathcal{K}(p, q) = \mathcal{K}(q, p).$$

Second, nontrivial symmetry with respect to transformation \mathcal{G} is

$$\mathcal{K}(p, q) = \mathcal{K}(-p + f(q), q).$$

To understand how this symmetry works, let us consider a closed invariant curve $\mathcal{K}(p, q) = \text{const}$ encompassing the fixed point (black curve in Fig. 2). Solving implicit equation $\mathcal{K}(p, q) = \text{const}$ for p results in two roots $p = \Phi(q)$ or $p = \Phi^{-1}(q)$, which correspond to the upper or lower branches in Fig. 2. Next, using the mapping equation (MH form of map) the reader can verify that the following important condition holds:

$$f(q) = \Phi(q) + \Phi^{-1}(q). \quad (2)$$

The condition (2) implies that the symmetry line $p = f(q)/2$ “splits” closed curve $\mathcal{K}(p, q) = \text{const}$ into two halves: the upper $\Phi(q)$ and lower $\Phi^{-1}(q)$ branches with the endpoints located at $\partial_q \Phi(q) = \pm\infty$. For each value of q where $\mathcal{K}(p, q) = \text{const}$ is defined, the upper and lower parts are equidistant from the second symmetry line

$$f(q)/2 - \Phi(q) = \Phi^{-1}(q) - f(q)/2.$$

McMillan wrote in regards to this condition: “*This is a remarkable result, of startling simplicity, which fell out almost without effort on my part. It leads to not just one, but to great families of functions $f(p)$ giving regions of stability. It also has a simple geometrical interpretation.*”

Here we would like to make two comments. (i) The origin of these two symmetries is due to the reversibility of symplectic maps [23]; any symplectic map with an inverse can be decomposed into two involutions similar to a map in the MH form with the integral of motion being invariant under both transformations. (ii) Both symmetries also hold for survived invariant tori in chaotic maps. Figure 2 illustrates symmetry properties for two classes of survived tori in Hénon map: a closed curve and a set of islands.

III. ONE-PIECE MAPS

In this section, we will consider mappings in the MH form with f being a simple linear function, $f(q) = kq$. We will refer to such mappings as *one-piece maps* or mappings with *linear force function*, purposely avoiding the term “linear map.” We will reserve the term *linear map* (in contrast to *nonlinear map*) to refer to the independence of dynamics on amplitude (i.e., the rotation number is independent on amplitude for all stable trajectories); mappings in the MH form with nonlinear force function can possess linear dynamics. To avoid confusion, we will follow the terminology established above. As we will see, all one-piece maps are integrable and linear.

A. Polygon maps with integer coefficients

According to *crystallographic restriction theorem* [24,25], if $A \in \text{SL}(2, \mathbb{Z})$ and $A^n = I_2$ for some natural $n \in \mathbb{N}$, where $I_2 = \text{diag}(1, 1)$ is an identity matrix, then the only possible solutions have periods $n = 1, 2, 3, 4, 6$, which corresponds to one-, two-, three-, four-, and six-fold rotational symmetries. Transformations with a period $n = 1, 2$ are simply $\pm I_2$, which can be considered as special cases of the rotation of the plane, $\text{Rot}(\theta)$, through the angles equal to $\theta = 0$ or π , respectively. Three other cases, $n = 3, 4, 6$, are given by mappings in the MH form

$$\alpha : \begin{cases} q' = p, \\ p' = -q - p, \end{cases} \quad \beta : \begin{cases} q' = p, \\ p' = -q, \end{cases} \quad \gamma : \begin{cases} q' = p, \\ p' = -q + p, \end{cases}$$

further referred to as α , β , and γ , respectively, and, with invariant polygons being concentric triangles, squares, and hexagons (see Fig. 3).

B. Fundamental polygons of the first kind

To understand the nature of invariant polygons from crystallographic restriction theorem, we first will consider a more

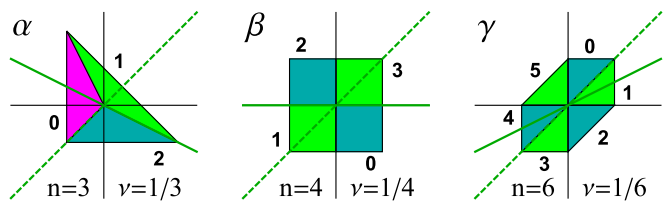


FIG. 3. Integer mappings with linear force function and polygon invariants α , β , and γ (we use the same naming convention as Refs. [26,27]). Note that the invariant triangle was modified to satisfy both symmetries. Each figure shows one invariant polygon, with each colored region i being mapped to region $i + 1$. Here n is the period and ν is the rotation number of the map, which represents the average increase in the angle per map iteration. The dashed and solid dark green lines show the first and second symmetry lines.

general one-piece map in the MH form

$$\begin{aligned} q' &= p, \\ p' &= -q + k p, \end{aligned} \quad (3)$$

where parameter $k \in \mathbb{R}$ is not restricted to integers. This map is known to be integrable with quadratic invariant of motion [14]

$$\mathcal{K}(p, q) = p^2 - k p q + q^2.$$

Mapping (3) is unstable for $|k| > 2$, that results in level sets of the invariant being hyperbolas. However, the mapping is stable for $|k| < 2$ with level sets corresponding to a family of concentric ellipses; see Fig. 4. Within the parameter range corresponding to stable maps, the rotation number ν is independent of the amplitude and given by $\nu = \arccos(k/2)/(2\pi)$.

Thus, one can see that if $\arccos(k/2)$ is incommensurate with π , the motion is quasi-periodic, and according to Kronecker’s density theorem, iterations starting from the initial condition (q_0, p_0) will result in points densely covering the ellipse $\mathcal{K}(p, q) = \mathcal{K}(p_0, q_0)$. However, if $\arccos(k/2)$ is commensurate with π , then the motion is strictly periodic and ν becomes a rational number. As a result, point (q_0, p_0) will return to its initial position after a finite number of iterations and will not depict an ellipse. In fact, linear mappings with rational ν are more than integrable, they possess *superintegrability*, meaning that they have more than one functionally independent invariant of motion $\mathcal{K}(p, q)$.

For example, for each map with rational $\nu \in \mathbb{Q}$, one can construct two sets of polygon invariants by iterating an initial point starting on the first, $p = q$, or second, $p = k q/2$, symmetry lines and using iterations as vertices (Fig. 5). We will refer to such polygons as *first and second sets of fundamental polygons of the first kind*; first or second sets refer to the position of the initial point on the first or second symmetry lines, respectively, and “the first kind” refer to the fact that the force function consists of one piece only. In the case of even period, two sets of polygons are actually different while for odd period sets, polygons are identical up to rotation by an angle π , $(q, p) \rightarrow (-q, -p)$. In the former case, the first set of polygons has no vertices on the second symmetry line (and two vertices on the first symmetry line) while the second set has no vertices on the first symmetry line (and two vertices on

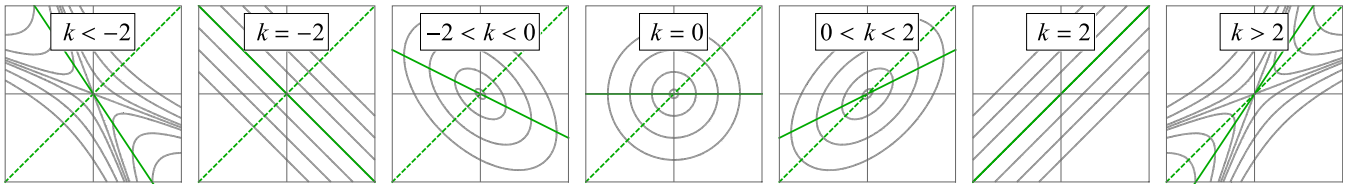


FIG. 4. Constant level sets of invariant for one-piece map in the MH form, $\mathcal{K}(p, q) = p^2 - k p q + q^2 = \text{const}$. For $|k| < 2$ the level sets are ellipses, for $|k| > 2$ the level sets are hyperbolas and for $|k| = 2$ they are parallel lines. The dashed and solid green lines are the first and second symmetry lines.

the second). In the latter case, both sets of polygons have a single vertex on each symmetry line.

The only integer values of k corresponding to stable mappings ($|k| < 2$) are $k \in \{-1, 0, 1\}$. For each integer value of parameter k , the value of $\arccos(k/2)$ (respectively, $2\pi/3$, $\pi/2$, and $\pi/3$) is commensurate with π , thus proving that maps α , β and γ are the only stable one-piece maps in the MH form with integer coefficients.

In addition, for $|k| = 2$ invariant level sets are straight lines. We will denote these mappings as “a” for $k = 2$ and “b” for $k = -2$. While being unstable, both maps have polygonal chains (connected series of line segments, in this case just the line itself) as its invariant. In the following sections, we will see that unstable and stable polygon maps can be combined together to form more complicated systems.

IV. TWO-PIECE MAPS

A. Linear mappings

1. Polygon maps with integer coefficients

Another remarkably interesting result is given by CNR Theorem (Cairns, Nikolayevsky, and Rossiter [26,27]). Suppose that \mathcal{M} is a periodic continuous mapping of the plane that is a linear transformation with integer coefficients in each

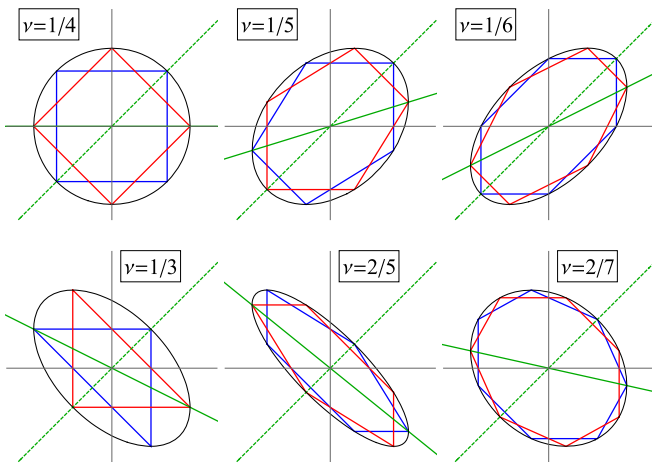


FIG. 5. Fundamental polygons of the first kind for different values of rotation number v . Each plot shows the invariant ellipse $\mathcal{K}(p, q) = p^2 - k p q + q^2 = \text{const}$ (black) and two invariant fundamental polygons inscribed into it (blue and red). The dashed and solid green lines correspond to the first and second symmetry lines.

half plane $q \geq 0$ and $q < 0$. Then \mathcal{M} has a period

$$n = 1, 2, 3, 4, 5, 6, 7, 8, 9, \text{ or } 12.$$

All maps discovered by Cairns and others are in the MH form with force function consisting of two linear segments

$$f(q) = q \times \begin{cases} k_1, & q < 0, \\ k_2, & q \geq 0. \end{cases} \quad (4)$$

In addition to previously described one-piece maps (trivial cases $k_1 = k_2$) with $n = 1, 2, 3, 4, 6$, now we have five more mappings with $n = 5, 7, 8, 9$ (Fig. 6). These maps are stable, linear and integrable, with polygons being their invariant sets, and denoted with capital Latin letters D–H. Note how Cairns, Nikolayevsky, and Rossiter rediscovered the Knuth map, H, from the first principles.

2. Fundamental polygons of the second kind

Similar to the case of one-piece mappings, to understand the origin of polygon invariants we should consider a less restricted map, corresponding to force function (4):

$$\begin{aligned} q' &= p, \\ p' &= -q + \frac{k_1 + k_2}{2} p + \frac{k_2 - k_1}{2} |p|, \end{aligned} \quad (5)$$

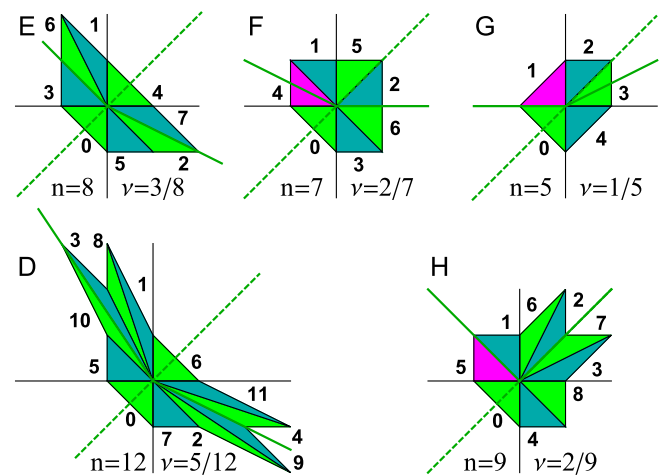


FIG. 6. Integer mappings with two-piece force function and polygon invariants D–H (named after [26]). Each figure shows one invariant polygon, with each colored region i being mapped to the region $i + 1$. Here n and v are the period and rotation number of the map. The solid and dashed dark green lines show the second and first symmetry lines.

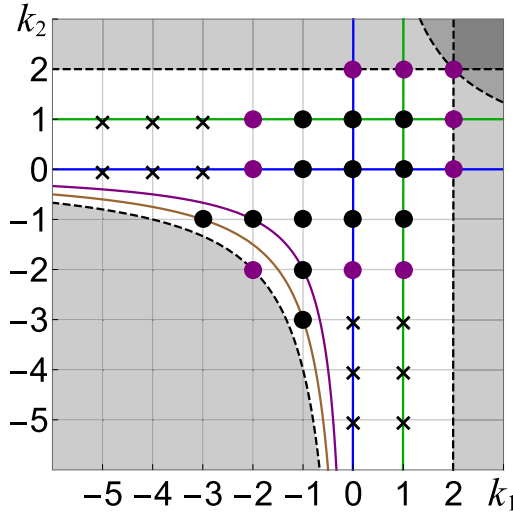


FIG. 7. The plane of parameters (k_1, k_2) for two-piece maps. The dashed lines show the area of global stability, $p, q < 2 \wedge pq < 4$: the map can be stable (but not necessarily) only within the area of stability, shown in white. The solid curves show all lines of “constant topology” passing through integer nodes $(k_1, k_2) \in \mathbb{Z}^2$ within the stable zone: the red line corresponds to a single ellipse $k_1 = k_2$, blue lines corresponds to two ellipses (McMillan beheaded and two-headed ellipse) $k_{1,2} = 0$, green lines refer to three ellipses defined by $k_{1,2} = 1$ and purple and brown hyperbolas are $k_1 k_2 = 2$ and $k_1 k_2 = 3$, respectively. Integer nodes corresponding to stable mappings with polygon invariants are shown in black, unstable mappings with an invariant being a polygonal chain in purple, and the remaining integer nodes within the global region of stability are shown with crosses (unstable maps with invariant consisting of hyperbolas).

where parameters $k_{1,2} \in \mathbb{R}$. This is a very nontrivial dynamical system considered in great detail in Refs. [28–31]. Here, we will provide some results contributing to our understanding of polygon maps.

(1) Map (5) is integrable.

(2) Map (5) is linear, i.e., there is no dependence of the rotation number on the amplitude. Since we are free to choose units of p and q , using scaling transformation ($\epsilon > 0$)

$$\begin{aligned} q' &= \epsilon q, \\ p' &= \epsilon p, \end{aligned}$$

one can reconstruct dynamics on any ray of initial conditions (starting at the origin) from a single trajectory.

(3) Dynamics of map (5) can be either stable or unstable depending on the values of $k_{1,2}$, that creates a nontrivial fractal area on the stability diagram (see Ref. [28] for more detail). While we are not considering the fine structure of the fractal area, we would like to note that all pairs (k_1, k_2) resulting in stable mappings are within the area defined by (Fig. 7)

$$p, q < 2 \wedge pq < 4 \text{ for } p, q < 0.$$

Stable maps are either periodic when the rotation number ν is rational or quasi-periodic for irrational ν .

(4) The invariant of motion is a combination of segments of ellipses, straight lines or hyperbolas “glued” together and

defined by

$$C_1 p^2 + C_2 p q + C_3 q^2 = \text{const.}$$

In the plane of parameters (k_1, k_2) there are *lines of constant topology*. Along these lines, the number of segments remains constant.

(5) For example, the simplest case corresponds to the family of one-piece maps, $k_1 = k_2$, (red line in Fig. 7). As we learned above, in this case the phase space consists of only one ellipse (or two sets of hyperbolas conjugate to each other) defined by

$$\mathcal{K}(p, q) = p^2 - k_1 p q + q^2.$$

As we move along the line $k_1 = k_2$, the ellipses bifurcate into hyperbolas at $k_1 = |2|$ and the trajectories lose stability.

(1) The next line of constant topology is given by $k_2 = 0$ and line $k_1 = 0$ corresponding to a family of twin maps, see blue solid lines in Fig. 7. This is the aforementioned beheaded and two-headed ellipses discovered by McMillan with the invariant defined by two ellipses glued together:

$$\mathcal{K}(p, q) = \begin{cases} p^2 + k_1 p q + q^2, & p, q \geq 0, \\ p^2 - k_1 p q + q^2, & \text{otherwise.} \end{cases}$$

Here is his explanation on how this map works: *In an earlier paragraph a promise was made that cases could be constructed with boundaries that more than double valued. I shall now fulfill the promise by describing a procedure by which this can be done. Take any known case with a center of symmetry at the origin, and erase the part of the boundary lying in the +, + quadrant. Replace $f(q)$ by $f(q) = 0$ to the right of the origin. Fill in the erased part of the boundary by reflecting the part in the +, - quadrant about the q axis. The resulting completed boundary is an invariant under the transformation with the original $f(q)$ to the left of the boundary, and $f(q) = 0$ to the right. Starting with ellipses, we can get beheaded ellipses (first row of Fig. 8, case $0 < k_1 < 2$) or double headed ellipses (first row of Fig. 8, case $-2 < k_1 < 0$), and here we see a four-valued function acting as an invariant boundary.* Note that to have only two ellipses as invariants of motion, the second ellipse has to be added to the +, + quadrant (or to -, - quadrant for twin maps with $k_1 = 0$). Otherwise, an addition of an ellipse into the +, - quadrant will result in its reflection in the quadrant -, + (due to the first symmetry line $p = q$), making the number of ellipses equal to three. In the case when the second segment of the force function has zero slope, $k_2 = 0$, the map in Eq. (5) is stable for $|k_1| < 2$ (see first row of Fig. 8). For the slopes $k_1 = \pm 2$ the invariant level sets become polygonal chains with one- and threefold symmetries, respectively. When stable, the rotation number is given by

$$\nu = \frac{\arccos(k_1/2)}{\pi + 2 \arccos(k_1/2)}.$$

As in the case $k_1 = k_2$, when $\arccos(k_1/2)$ is commensurate with π , we have a rational rotation number $\nu \in \mathbb{Q}$ resulting in a periodic map. The only integer values of k_1 satisfying this condition are $k_1 \in \{-1, 0, 1\}$ (mappings F, β , and G, respectively).

In fact, this line of constant topology is just one of many defined by $k_2 = 2 \cos(\pi/n)$ for $n \geq 2$. On each line the map is

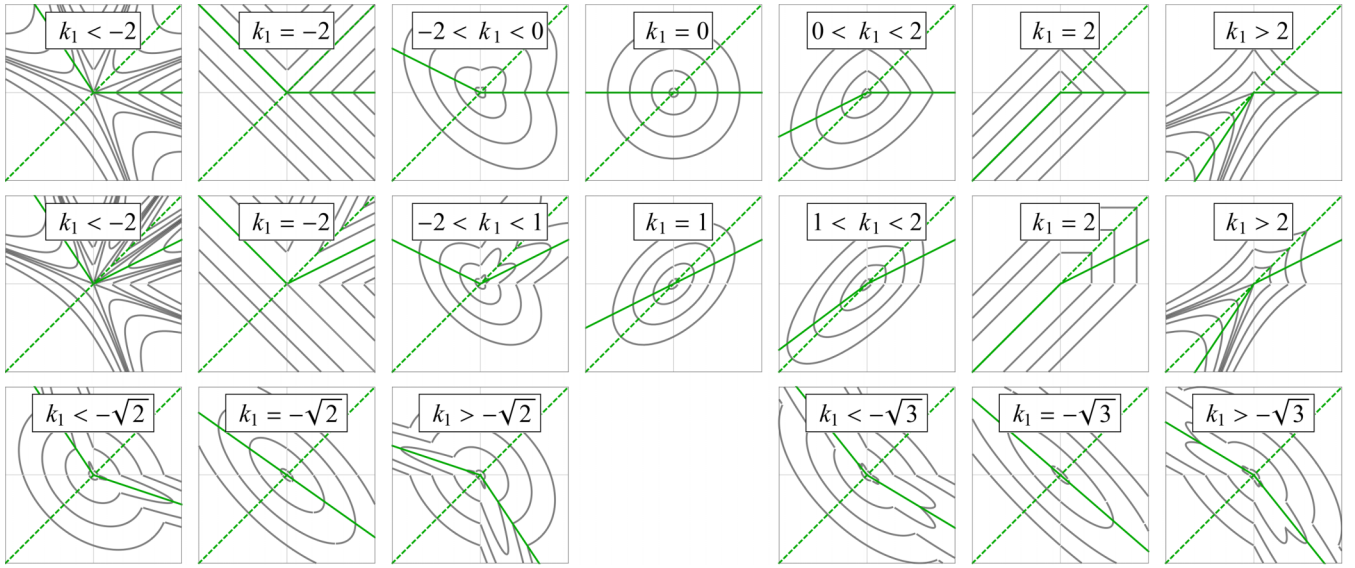


FIG. 8. Invariant level sets along lines of constant topology for a two-piece map in the MH form. The first and second rows illustrate the transformation of the invariant for cases $k_2 = 0$ and $k_2 = 1$ (blue and green lines in Fig. 7). The three left plots in the third row show bifurcation along hyperbola $k_1 k_2 = 2$ and the three right plots are for $k_1 k_2 = 3$ (purple and brown hyperbolas in Fig. 7). The solid and dashed green lines are the second and first symmetry lines.

stable for $|k_1| < 2$, it produces a polygonal chain as invariant for $k_1 = \pm 2$ and when stable, has a rotation number

$$v = \frac{\arccos(k_1/2)}{\pi + n \arccos(k_1/2)}.$$

Along each line of constant topology, the invariant consists of n ellipses (hyperbolas) with $n - 1$ of them in the first quarter.

Among these lines, there is another line we should focus on: case $n = 3$ with $k_2 = 1$ (and twin $k_1 = 1$). As we can see, in addition to line $k_2 = 0$, this is the only line with integer k_1 . The invariant of motion is

$$\mathcal{K}(p, q) = \begin{cases} p^2 - (2 - k_1)(p q - q^2), & p > q > 0, \\ (2 - k_1)(p^2 - p q) + q^2, & 0 < p < q, \\ p^2 - k_1 p q + q^2, & \text{otherwise,} \end{cases}$$

second row of Fig. 8. From this line we have two more mappings with polygonal chain ($k_1 = \pm 2$) and three periodic maps with integer coefficients ($k_1 = -1, 0, 1$, i.e., maps α , F and H).

(1) As one can notice, lines $k_1 = k_2$ and $k_{1,2} = 0, 1$ are covering most integer nodes $(k_1, k_2) \in \mathbb{Z}^2$ within the area of global stability (see Fig. 7). The remaining nodes belong to two lines of constant topology from the family given by $k_1 k_2 = 4 \cos^2(\pi/(2n))$ with $k_{1,2} < 0$ and $n \geq 2$. Those lines are for $n = 2$ and 3. Along those lines, the map is always stable and periodic with the rotation number $v = (2n - 1)/(4n)$. The invariant of motion consists of segments of $(2n - 1)$ different ellipses: the central ellipse, $(n - 1)$ ellipses in II quadrant, and another $(n - 1)$ in IV quadrant (placed symmetrically with respect to $p = q$). For example, for $n = 2$ the invariant is

$$\mathcal{K}(p, q) = \begin{cases} p^2 - \left(\frac{4}{k_1} - k_1\right) p q + \left(\frac{4}{k_1^2} - k_1\right) q^2, & p > q > 0, \\ \left(\frac{4}{k_1^2} - k_1\right) p^2 - \left(\frac{4}{k_1} - k_1\right) p q + q^2, & 0 < p < q, \\ p^2 - k_1 p q + q^2, & \text{otherwise.} \end{cases}$$

Third row of Fig. 8 illustrates this case. For $k_{1,2} = -1$ from lines $n = 2, 3$ we have two remaining periodic maps with integer coefficients, E and D .

Thus, similar to the case of the one-piece map (degenerate line $k_1 = k_2$), we can define *fundamental polygons of the second kind*: for each line of constant topology, its stable maps with a rational rotation number are degenerate and have more than one invariant of motion including polygons. In contrast to the case $k_1 = k_2$, when we had two sets of polygons, now we only have a single set of fundamental polygons. These polygons have two vertices on the second symmetry line for maps with an even period or a single vertex on both symmetry lines for odd periods. Figure 9 shows a few examples of this degeneracy illustrating fundamental polygons of the second kind inscribed in an alternative invariant set of ellipses. Note that the first example is for the Brown-Knuth map showing an alternative three-headed ellipse which is also an invariant of motion.

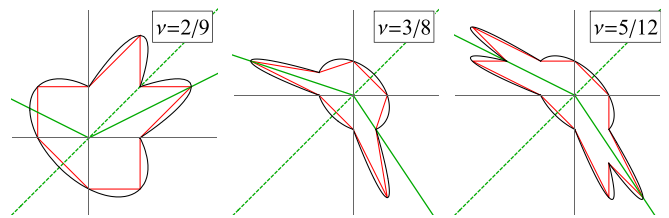


FIG. 9. Shapes of fundamental polygons of the second kind corresponding to different families of maps represented in Fig. 7. Each plot shows invariant ellipses (black) and invariant polygons inscribed into it (red). From left to right: line $k_2 = 1$ for $k_1 = -1$ (Brown-Knuth map, H), line $k_1 k_2 = 2$ for $k_1 = -1$, line $k_1 k_2 = 3$ for $k_2 = -3$ (map E). The dashed and solid green lines correspond to the first and second symmetry lines.

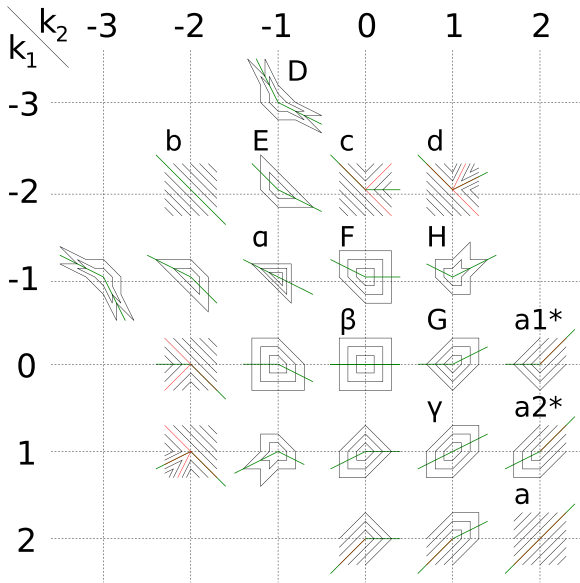


FIG. 10. Integer linear mappings with two-piece force function and polygon invariants (stable and unstable maps). The black polygons (or polygonal chains for unstable mappings) show constant level sets of the invariant, red level sets are separatrix for unstable mappings with stable periodic dynamics, and the green line is the second symmetry line.

3. Ingredients of mappings with polygon invariant

Hereby, one can see that there is one condition and two mechanisms determining polygon shapes (including unstable mappings with the invariant level set being a connected series of line segments—nonintersecting polygonal chains). The condition is that the force function f should be in a piecewise linear form that follows from the second symmetry: the sum of vertically opposed polygon sides is proportional to the value of the force function. The two mechanisms are:

(1) *Superintegrability in linear maps*. The rational rotation number causes degeneracy when more than one invariant of motion exists, including polygons (e.g., fundamental polygons of the first and second kind).

(2) *Loss of stability*. Ellipses are transitioned to hyperbolas via the straight lines in linear two-piece maps, e.g., see cases $|k_1| = 2$ for the first two rows in Fig. 8.

These mechanisms are respectively responsible for stable and unstable polygons. As we will see further, more complicated nonlinear mappings with polygon invariants can be constructed, but at lower $[(q, p) \rightarrow 0]$ or higher amplitudes $[(q, p) \rightarrow \infty]$, they reduce to one of the already described transformations; we will observe that both mechanisms can be combined in one map resulting in very nontrivial dynamics. Below, in Fig. 10 we illustrate all integer linear mappings with two-piece force function and polygon invariants (stable and unstable).

B. Nonlinear mappings

Here we begin our exploration of *nonlinear* symplectic mappings. So far we considered only mappings with force function in the form (4). The simplest modification we can

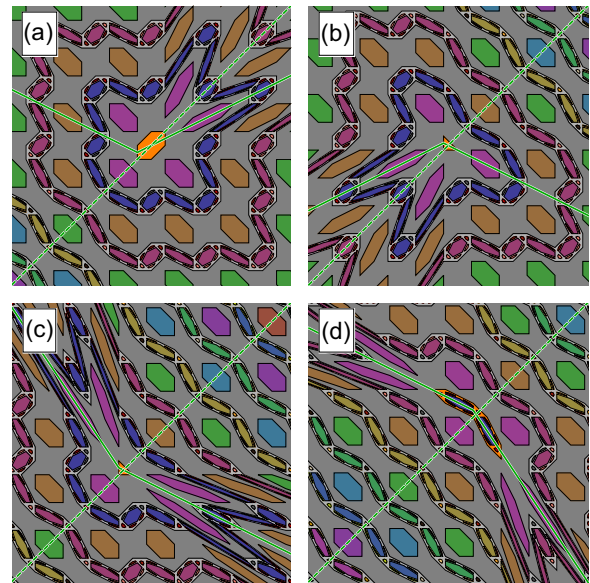


FIG. 11. Zoo maps: Gingerbreadman (a), Rabbit (b), Octopus (c), and Crab (d) mappings. The light and dark gray areas represent alternating zones of instability which are sectioned by two families of concentric invariant polygons resembling animals. Within each zone of instability there are three different scenarios. First, orbits that result from initial conditions $(q_0, p_0) \in \mathbb{Q}$. Those are stable orbits with an exact periodic motion and rational rotation number resulting in an invariant set of points. The second scenario includes all other initial conditions within the gray zones with any or both q_0, p_0 being irrational, $q, p_0 \in \mathbb{R} \setminus \mathbb{Q}$. Those are chaotic orbits never returning to initial conditions and densely covering the zone of instability. The third and last scenario is for any initial condition within the colored regions of phase space. Those are *chains of linear islands*; the initial condition from these regions of phase space hops from island to island of the same group (each group is shown with its own color related to the relative orbit period). Such initial condition returns to itself and the motion is strictly periodic with the rotation number being *mode-locked* within the island. To view an “animal” you must rotate each image 135 degrees clockwise.

make is to add a constant *shift parameter*, d :

$$f(q) = \frac{k_1 + k_2}{2} q + \frac{k_2 - k_1}{2} |q| + d.$$

The map becomes nonlinear and we cannot reconstruct dynamics along the ray of initial conditions using scaling transformation $(q, p) \rightarrow \epsilon(q, p)$, $\epsilon > 0$. Instead, now we have a choice of natural units $\epsilon = d$, and one can show that without the loss of generality for two-piece maps, d can be restricted to ± 1 or 0.

The introduction of d not only adds the dependence on amplitude, but might result in a loss of integrability causing chaotic behavior. A famous example is the Gingerbreadman [32] map—a chaotic two-dimensional map in the MH form with $f(q) = |q| + 1$ (see first plot in Fig. 11). The remarkable property of this map is that some invariant tori survived perturbation and after deformation remained polygons. The chaotic dynamics is sectioned by concentric polygons making this map the simplest model for area-preserving twist mappings

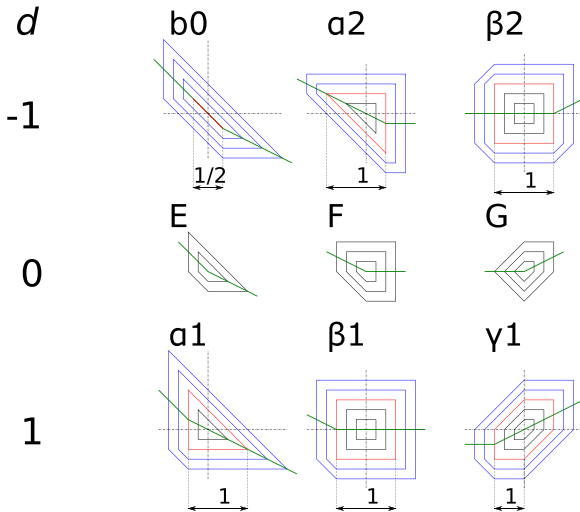


FIG. 12. Integer nonlinear integrable maps with polygon invariants and two-piece force function. The top and bottom rows of the figures show level sets of the invariant for $d = \mp 1$. The middle row shows cases for $d = 0$, and, in each column the transformations have the same slopes $k_{1,2}$ as for $d = 0$ (see Fig. 10); note that the invariant level set of the outer nonlinear layer at the large amplitude is asymptotic to the level set of the corresponding map. The black (blue) level sets are linear (nonlinear) trajectories. The red level sets represent the separatrix isolating the inner linear from the outer nonlinear layers. The green line shows the second symmetry line, $p = f(q/2)$.

with zones of instability. It shares many properties of the smooth mappings and has an advantage of having an exact arithmetic on rational numbers. Another mapping we would like to mention here is the *Rabbit* map for $f(q) = |q| - 1$. To the best of our knowledge, this map has not been mentioned before, but we are certain that Robert Devaney, the discoverer of Gingerbreadman, knew about it due to the close connection between the maps (second plot in Fig. 11).

1. Zoo mappings

After reading the article of Cairns, Nikolayevsky, and Rossiter [26], our first idea, which predetermined discoveries made in this article, was to produce objects similar to Devaney map using newly discovered mappings D–G. First we tried mapping D, and amazingly, it worked! We introduce two new dynamical systems, the *Octopus* and the *Crab* mappings for $f(q) = |q| - 2q \pm 1$, respectively [33] (last two plots in Fig. 11). Informally, we grouped them together with the Rabbit and Gingerbreadman, and, called them *zoo maps*. The mappings are again chaotic and “sectioned” by infinitely many concentric invariant polygons. The basic dynamics of these maps are described in the caption to Fig. 11.

2. Nonlinear integrable maps with polygon invariants

When $d = \pm 1$, not all mappings experience chaotic behavior like Gingerbreadman or zoo maps. Unexpectedly, transformations E, F, and G produced nonlinear integrable systems with polygon invariants if the vertical shift parameter d is added [33] (see Fig. 12). Since $d \neq 0$, the fixed point

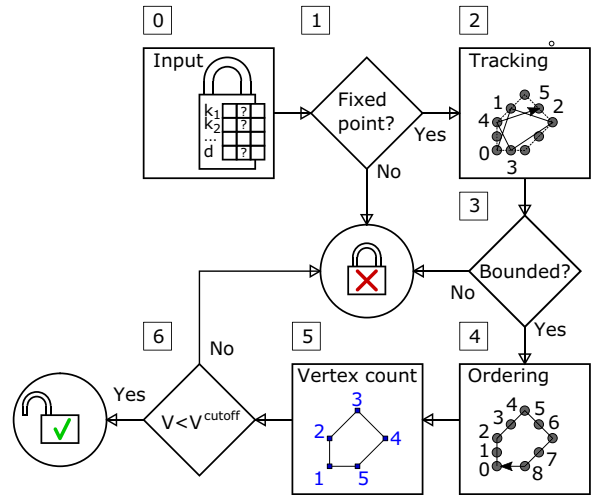


FIG. 13. Flowchart representing the machine-assisted discovery of integrable maps. The algorithm verifies if the map defined by the input (0) is integrable with the invariants being concentric polygons. If the map has a fixed point (1), then the algorithm performs tracking for different initial conditions (2), and if all orbits are bounded (3), then it proceeds to the construction of orbit polygons via ordering (4). Finally, after counting the number of vertices V (5), if for each polygon $V < V^{\text{cutoff}}$, then the map is sent for analytic verification. The search process terminates when any conditional operation is false (NO).

moves from the vertex to one of the linear pieces (depending on the sign of d) of the force function. As a result, the area of mode-locked motion around the fixed point is formed with the invariant level sets being triangles, squares, hexagons or line segment $p = -q$ with period 2 for map b0. For larger amplitudes, the motion is still integrable, but the rotation number becomes amplitude dependent (trajectories shown in blue). The inner linear and outer nonlinear layers are separated by a separatrix matching the dynamics (shown in red). The dynamical properties for all mappings are listed in Table I as functions of amplitude along q axis x .

V. MACHINE-ASSISTED DISCOVERY OF INTEGRABLE MAPS WITH POLYGON INVARIANTS

After discovering six nonlinear polygon maps shown in Fig. 12 and performing a few more numerical experiments, we realized that the force function can be further generalized to have $n > 2$ linear segments, potentially producing new families of integrable systems. To automate the search, we designed a relatively simple algorithm that finds integrable mappings based on the analysis of individual trajectories; first, we verified some of its principles in Ref. [34], and then we significantly modified it and performed an extensive search.

A. Search algorithm

The detailed pseudocode of the search algorithm is presented in Appendix B and its Python implementation is available at Ref. [35]. The algorithm is illustrated via flowchart in Fig. 13 and its blocks with processes and decisions are described below.

TABLE I. Dynamical properties of integer nonlinear integrable mappings with polygon invariants and two-piece force function. Here v_0 is the rotation number in the inner linear layer, v_1 , J_1 , and J'_1 are, respectively, rotation number, action, and partial action in the outer nonlinear layer, x is the linear amplitude in a nonlinear layer defined as the horizontal or vertical distance from the separatrix to the trajectory under consideration.

Map	v_0	v_1	J_1	J'_1
b0	$\frac{1}{2}$	$\frac{1+3x}{2+8x}$	$4x^2 + 2x$	$\frac{3}{2}x^2 + x$
$\alpha 1$	$\frac{1}{3}$	$\frac{1+3x}{3+8x}$	$4x^2 + 3x + \frac{1}{2}$	$\frac{3}{2}x^2 + x + \frac{1}{6}$
$\alpha 2$	$\frac{1}{3}$	$\frac{1+2x}{3+7x}$	$\frac{7}{2}x^2 + 3x + \frac{1}{2}$	$x^2 + x + \frac{1}{6}$
$\beta 1$	$\frac{1}{4}$	$\frac{1+2x}{4+7x}$	$\frac{7}{2}x^2 + 4x + 1$	$x^2 + x + \frac{1}{4}$
$\beta 2$	$\frac{1}{4}$	$\frac{1+x}{4+5x}$	$\frac{5}{2}x^2 + 4x + 1$	$\frac{1}{2}x^2 + x + \frac{1}{4}$
$\gamma 1$	$\frac{1}{6}$	$\frac{1+x}{6+5x}$	$\frac{5}{2}x^2 + 6x + 3$	$\frac{1}{2}x^2 + x + \frac{1}{2}$

0. **Input.** We decided to focus on piecewise linear forces with integer coefficients, $f(q, \mathbf{k}, \mathbf{l}, d)$ with integer vectors \mathbf{k} , \mathbf{l} and d . While we performed a scan only for integer slopes \mathbf{k} , we were able to analytically generalize some of the results for more general values of the shift parameter $d \in \mathbb{R}$ and lengths of segments $l_i \in \mathbb{R}^+$.

1. **Fixed point.** For a map to be *stable*, i.e., all phase space orbits are bounded, it should have at least one fixed point $\zeta^* = (q^*, p^*)$. Mappings that do not have a fixed point, $\forall q \in \mathbb{R} : q \neq f(q)/2$, are out of scope.

2. **Tracking.** If a map is selected, then we trace out its orbits $\vec{\zeta} = (\zeta_1, \dots, \zeta_N)$ for different initial conditions $\zeta_0 = (q_0, p_0)$.

3. **Stability.** Mappings with a fixed point still can have unstable trajectories at larger amplitudes. If for some initial condition we detect an unbounded growth of the radial distance from the fixed point, $\exists i : |\zeta_i - \zeta^*| > r_{\max}$, then the map is excluded from further analysis.

4. **Ordering.** At the next stage, the points of each individual trajectory are ordered according to their polar angle $\phi = \arctan[(p - p^*)/(q - q^*)]$, such that the angle ϕ is monotonically increasing. After arranging the trajectory points according to ϕ we join the consecutive points resulting in an *orbit polygon*.

5. **Vertex count.** To count the number of vertices, V , for each orbit polygon we use scalar products of two vectors built on three consecutive points ($\mathbf{v}_1 = \zeta_i - \zeta_{i-1}$ and $\mathbf{v}_2 = \zeta_{i+1} - \zeta_i$),

$$V = \sum_i \theta(\alpha_i - 1), \quad \alpha_i = \frac{\mathbf{v}_1 \cdot \mathbf{v}_1}{|\mathbf{v}_1||\mathbf{v}_2|},$$

where $\theta(x) = \mathbf{1}_{x>0}$ is a Heaviside step function. In numeric experiments, when $\mathbf{v}_1 \parallel \mathbf{v}_2$, the normalized scalar product might be slightly different from unity, so a small cutoff parameter should be introduced, $\epsilon < |(\mathbf{v}_1 \cdot \mathbf{v}_2)/(|\mathbf{v}_1||\mathbf{v}_2|) - 1|$.

6. **Vertex cutoff.** At the final stage we are left with stable integrable or chaotic maps which we would like to separate. The key insight is that we are looking for transformations with all invariant tori being polygons and assume that the phase space consists of concentric layers; in each layer the orbit polygons have the same finite number of vertexes which remains bounded when increasing the number of iterations $N \rightarrow \infty$. Conversely, for a chaotic trajectory, the number of

vertices linearly grows with the number of iterations, $V = \mathcal{O}(N)$. Such drastic difference in the growth of V with the iteration number allows us to automatically separate between the two cases. In a numeric experiment, we check that for all initial conditions the number of vertices is bounded by some cutoff parameter, $V < V^{\text{cutoff}} \leq N$.

In addition, for each mapping found by the search algorithm, we manually verify the McMillan integrability condition, thus rigorously proving their integrability. Although the search algorithm described here is quite powerful, there are some caveats to bear in mind:

(1) Maps with strongly nonconvex layers of polygon invariants can be missed by the algorithm. In cases when the orbit polygon is not convex with respect to the fixed point (q^*, p^*) , the points of the trajectory cannot be ordered according to the polar angle. While we do not have a particular example, we should keep it in mind.

(2) Inside integrable nonlinear layers fibrated with polygons there are two types of orbits: those with rational and those with irrational rotation numbers. The latter are quasi-periodic with the entire polygon being densely covered. However, the former are strictly periodic with the orbit visiting only a finite number of points, thus potentially showing a smaller number of vertexes. All rotation numbers within a layer are in the form $v(q_0) = (\alpha + \beta q_0)/(\gamma + \delta q_0)$, where α, β, γ , and δ are integer parameters. To avoid periodic orbits which complicate the analysis, we can add a small irrational perturbation η to all initial conditions, $q_0 \rightarrow q_0 + \eta$. In fact, from this formula, one can see that in numeric experiments all observed orbits are periodic. This is not a problem as long as the period is sufficiently large compared to the number of polygon sides, so the points of orbit visit all sides of the polygon covering them densely enough.

(3) Finally, while we've been only looking for maps with invariant layers being concentric polygons, while phase space can involve polygon islands. In the case of completely mode-locked islands (*linear islands*) with all orbits visiting each island only once, our algorithm will successfully handle this case. But in the case of nonlinear islands (i.e., a trajectory visits sequentially each island under iterations and traces out invariant tori around centers of islands) our algorithm indeed will fail; as in the case of nonconvex polygons, the points of orbit cannot be arranged by the polar angle since now they are a multiple valued function.

B. Search results

To construct more complex piecewise linear symplectic maps one can add more segments to the force function f . When the number of segments is equal to three, in total we have four parameters: three slopes $k_{1,2,3}$ and a shift parameter d . By performing the rescaling of coordinates, one can see that without loss of generality, the length of the middle segment can always be assumed to be equal to one. In addition, unlike the case of the two-piece force function when $d = 0, \pm 1$, now the shift parameter belongs to reals.

For the force function with four pieces, the addition of an extra segment results in a total of six parameters: four slopes $k_{1,2,3,4}$, shift parameter d and ratio $r = l_2/l_3$; the scale transformation allows us to normalize one of two finite pieces (l_2 or l_3) to unity so only one of them is independent.

We performed the search for three- and four-piece integer force functions using our algorithm across a wide range of the parameter values. The integer valued slopes of the segments of the force function are selected from the range $-10 \leq k_i \leq 10$ and the shift parameter $-50 \leq d \leq 50$. In the case of four-piece maps, the ratio of the lengths of segments were selected in the range $r \in [1/10, 1/9, \dots, 1, 2, \dots, 10]$. However, the search space can be further reduced when relying on our prior knowledge about the properties of piecewise linear mappings with two segments, which approximate a generic n -piece mapping at small or large amplitudes. Since integer two-piece maps with polygon invariants are confined to $-3 \leq k_{1,2} \leq 2$, the values of the slopes of the outer segments can be restricted to the same range. Similarly, in the vicinity of the fixed point (q^*, p^*) the mapping behaves as a single-piece or two-piece map (depending on whether the fixed point belongs to the segment of the force function or coincides with one of the vertexes separating adjacent segments) allowing reduction of possible values of $k_{1,2}$.

The values of the shift parameter d and the length ratio r are less restrictive, because they are only responsible for the position of the fixed point. While we performed a scan only

$$\begin{aligned} n = 2 : \quad & \frac{k_1 + k_2}{2} q + \frac{k_2 - k_1}{2} \sqrt{q^2 + \epsilon^2} + d \xrightarrow{\epsilon \rightarrow 0} d + q \times \begin{cases} k_1, & q < 0, \\ k_2, & q \geq 0, \end{cases} \\ n = 3 : \quad & \frac{k_1 + k_3}{2} q + \frac{k_2 - k_1}{2} \sqrt{q^2 + \epsilon^2} + \frac{k_3 - k_2}{2} \sqrt{(q-1)^2 + \epsilon^2} - \frac{k_3 - k_2}{2} + d \xrightarrow{\epsilon \rightarrow 0} d + q \times \begin{cases} k_1, & q < 0, \\ k_2, & 0 \leq q < 1, \\ k_3, & q \geq 1, \end{cases} \\ \dots & \dots \end{aligned}$$

Figure 16 shows examples of how the “smoothening” procedure can be used to produce new nearly integrable systems. More importantly, in addition to being near integrable, these mappings are stable since the limiting polygon at larger amplitudes provides an isolating integral.

Note that from a practical standpoint, the fact that produced systems are quasi- and not exactly integrable is not a problem as long as ϵ is sufficiently small and the chaotic formations are within the needed tolerances. Even if a system is originally designed as integrable, small errors (e.g., rounding errors for simulations, or tolerance errors for physical experimental setups) will destroy integrability on a small scale. Also, the

for integer d and r we were able to analytically generalize some of these results for $d \in \mathbb{R}$ and $r \in \mathbb{R}^{(+)}$.

Figure 14 presents most, but not all, mappings discovered by the search algorithm. They are grouped by a similarity of dynamics around the fixed point while arrows are pointed toward systems with more segments in f , thus showing hierarchy. The values of parameters for all discovered systems are listed in Appendix C.

VI. APPLICATIONS OF MAPPINGS WITH POLYGON INVARIANTS

A. Near-integrable systems

Since the force function is piecewise linear and is not smooth (not differentiable at a discrete set of points), it might seem that these polygon mappings are somewhat impractical. However, the polygon mapping can be smoothed using some parameter ϵ . Below we will demonstrate how one can construct not integrable, but quasi-integrable systems. One of the possible ways to perform this was first done by Cohen [36,37] in an application to the Brown-Knuth map (map H) by introducing a new force function as

$$f(q) = \sqrt{q^2 + \epsilon^2} \xrightarrow{\epsilon \rightarrow 0} |q|.$$

As one can see, it tends to $|q|$ as $\epsilon \rightarrow 0$ or at large amplitudes as $q \rightarrow \infty$. Figure 15 shows a comparison between Cohen and Brown-Knuth maps. Looking at the tracking results, one can see that new $f(q)$ produces a system with surprisingly regular behavior. However, detailed numerical experiments reveal multiple island structures at small scales [see Fig. 15 case (c)], indicating that an analytic invariant does not exist.

Thus, in a similar manner, one can first rewrite a general n -piece linear function using one linear and $(n-1)$ modulus function in the form $k_i|q - q_i|$ where q_i is a location of i th vertex, then substitute all modulus with square roots $k_i|q - q_i| \rightarrow k_i[(q - q_i)^2 + \epsilon^2]^{1/2}$, resulting in $f(q)$:

square root function is only one of the infinitely many ways of smoothing the force function (e.g., one can use \arctan , \tanh or others) and is used here as an example.

B. Discrete perturbation theory

Finally, knowledge of all possible integrable mappings with polygon invariants will not only help to construct new near integrable systems, but to understand the dynamics and phase space of more general nonintegrable mappings with smooth $f(p)$. This can be done by discretizing $f(p)$ by a piecewise linear function; so we have a

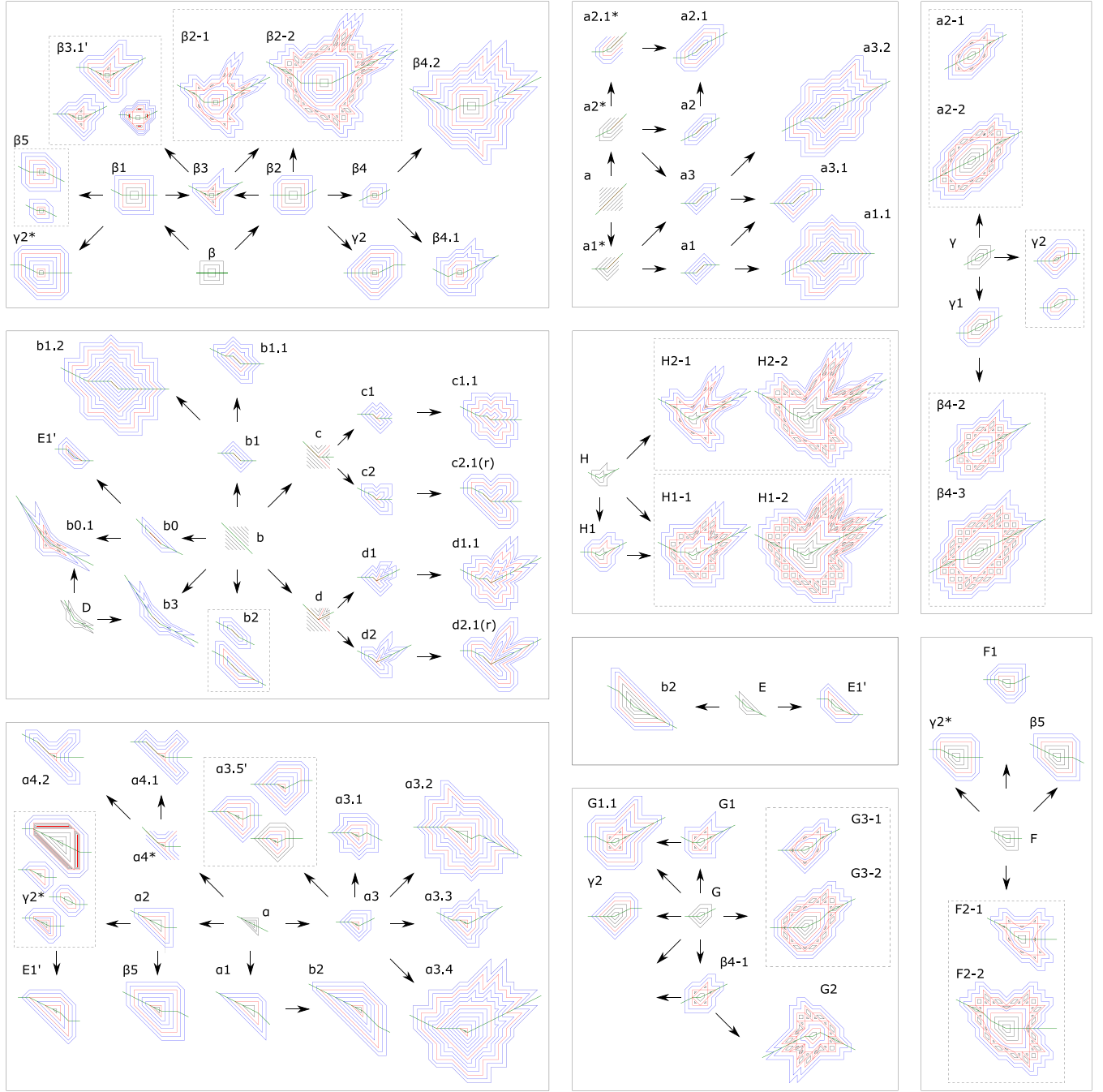


FIG. 14. Most (but not all) mappings discovered by an algorithm: one- through four-piece force functions. Maps are organized by dynamics around the fixed point; systems with the same rotation number around the fixed points are presented in the same solid box. The dashed boxes indicate that the map belongs to a discrete or continuous family.

perturbation theory where the order is determined by the number of pieces and the smallness parameter is defined by the smallest piece of the force function. To demonstrate the idea, we provide a comparison of a phase space for chaotic quadratic

$$f(p) = aq + q^2$$

and cubic Hénon maps

$$f(p) = ap + q^3$$

around specific resonances ($\nu = 1/4$ and stop band $\nu = 1/2$) and corresponding polygon maps. As one can see in Fig. 17 below, even low order approximations can reveal important qualitative dynamical features, including the shapes of trajectories in phase space and the topological structure of the phase portrait.

An interesting observation can be made looking at the *smaller alignment index* (SALI) color maps. SALI is an indicator (alternative to traditional maximal Lyapunov exponent) distinguishing between ordered and chaotic motion [38].

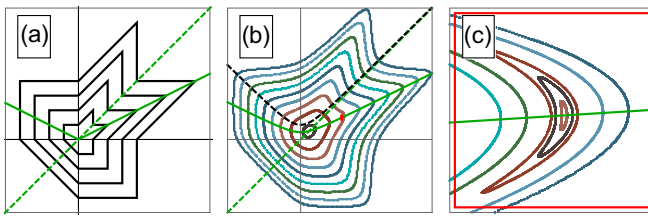


FIG. 15. The left plot (a) illustrates invariant level sets for the Brown-Knuth map, force function $f(q) = |q|$. The middle plot (b) displays invariant level sets for the Cohen map, $f(q) = \sqrt{q^2 + 1}$. The right plot (c) again provides invariant level sets for the Cohen map, but on a different scale showing one of the island structures. The level sets for Cohen map are obtained by tracking. The green curve is the second symmetry line $p = f(q)/2$.

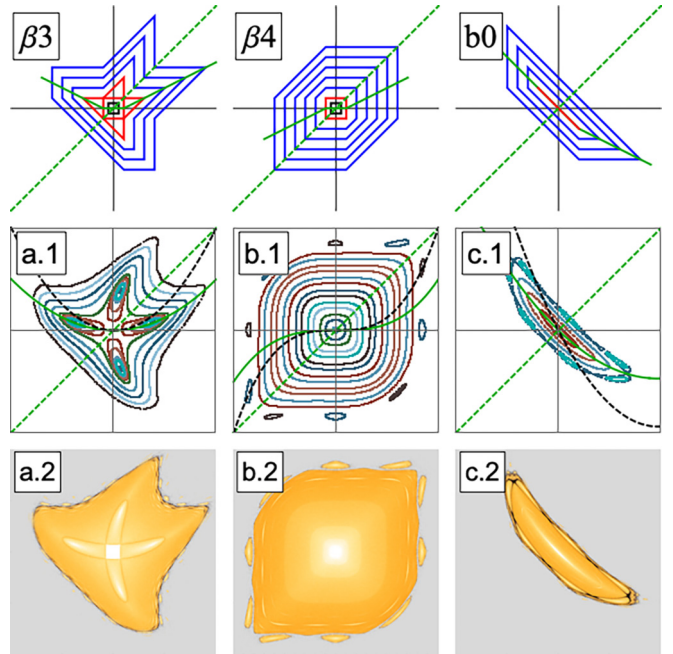


FIG. 17. The middle row of plots (a.1)–(c.1) shows tracking for Hénon map with quadratic $f(q) = aq + q^2$ [cases (a) and (c)], and cubic force functions $f(q) = aq + q^3$ [case (b)]. The value of parameter is (a) $a = a_{1/4} - 0.005$, (b) $a = a_{1/4} + 0.005$, and (c) $a = a_{1/2} + 0.05$, where $a_{1/4} = 0$ is the main octupole resonance with $v = 1/4$ and $a_{1/2} = -2$ is the linear-half integer stopband $v = 1/2$. The green curve is the second symmetry line $f(q)/2$ and the black dashed curve is the force function $f(q)$. All plots correspond to a range $p, q \in [-1, 1]$. The top row shows corresponding low order approximation via mappings with polygon invariants. The bottom row of plots (a.2)–(c.2) shows log of SALI values for the same cases, by courtesy of Ivan Morozov (BINP).

VII. SUMMARY

In this article, we presented an algorithm for the automated discovery of new integrable symplectic maps of the plane with polygon invariants, and as a result, we reported over 100 new integrable families. The algorithm successfully rediscovered some famous ultradiscrete Painlevé equations (see Appendix A for details) as well as some of the McMillan-Suris integrable maps.

While the discovered systems have a piecewise linear force and polygon invariants, thus lacking differentiability, we suggested a “smoothening” procedure which can produce new quasi-integrable systems without singularities. Such “smooth” polygon maps have potential applications in physics, engineering, dynamical system theory, and signal processing. For example, in accelerator physics, such near-integrable systems could reduce unwanted particle losses in accelerators and, thus, improve their performance and the achievable beam intensities. So far, the design of integrable accelerator focusing systems is at its very beginning, even conceptually. Fermilab presently operates the first accelerator [39], designed to test some of these concepts.

Finally, we introduced a discrete perturbation theory to relate our polygon mappings to a general symplectic map of a plane. The theory furthers our understanding of shapes

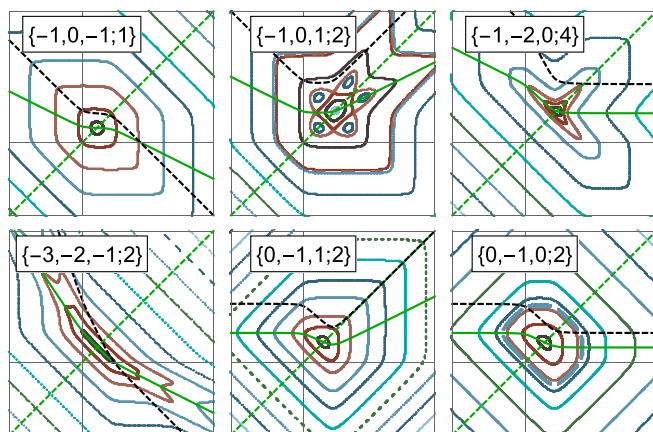


FIG. 16. Examples of quasi-integrable systems produced by “smoothening” three-piece integrable polygon maps using $\epsilon = 0.05$. For each plot the label shows parameters $\{k_1, k_2, k_3; d\}$. All level sets are obtained by tracking. The green curve is the second symmetry line $f(q)/2$ and the black dashed curve is the force function $f(q)$.

of phase space curves and approximates dynamics for more realistic chaotic systems such as Hénon or Chirikov mappings or even integrable ones, such as McMillan-Suris maps.

It remains an open question whether one can understand the totality of all maps with polygon invariants, and not only corresponding to force functions with integers coefficients. For example, it is not clear whether there exists some sort of generating formula which would allow us to derive integrable maps with $n + 1$ piece force function from mappings with n -pieces.

ACKNOWLEDGMENTS

The authors thank Eric Stern (FNAL) and Taylor Nchako (Northwestern University) for carefully reading this manuscript and for their helpful comments. Moreover, we extend our gratitude to Ivan Morozov (BINP) for multiple discussions and his generous contributions in preparation of Sec. VI B and especially Fig. 17. Finally, we express our deep appreciation for Nikolay Kuropatkin's (FNAL) useful discussion on the vertex count of polygons. Y.K. acknowledges funding by the DoE ASCR Accelerated Research in Quantum Computing program (Award No. DE-SC0020312), DoE QSA, NSF QLCI (Award No. OMA-2120757), NSF PFCQC program, DoE ASCR Quantum Testbed Pathfinder program (Award No. DE-SC0019040), U.S. Department of Energy Award No. DE-SC0019449, AFOSR, ARO MURI, AFOSR MURI, and DARPA SAVaNT ADVENT. Fermi National Accelerator Laboratory (Fermilab) is operated by Fermi Research Alliance, LLC. for the U.S. Department of Energy under Contract No. DE-AC02-07CH11359.

APPENDIX A: CONNECTION TO PAINLEVÉ EQUATIONS AND SURIS MAPPINGS

Some integrable mappings with polygon invariants have a direct connection to discrete Painlevé equations (dP). Painlevé equations are nonlinear difference equations with canonical form being [11,12]:

$$\begin{aligned} dP_I : \quad X_{n+1} X_{n-1} &= \frac{\lambda^n X_n + 1}{X_n^\sigma}, \quad \sigma = 0, 1, 2, \\ dP_{II} : \quad X_{n+1} X_{n-1} &= \frac{\alpha(\lambda^n + X_n)}{X_n^\rho(1 + \lambda^n X_n)}, \quad \rho = 0, 1, \\ dP_{III} : \quad X_{n+1} X_{n-1} &= \frac{(X_n + \alpha \lambda^n)(X_n + \alpha^{-1} \lambda^n)}{(1 + \beta \lambda^n X_n)(1 + \beta^{-1} \lambda^n X_n)}. \end{aligned} \quad (A1)$$

We will be interested in the *autonomous* (i.e., mappings do not have explicit dependence on n) limit of dP_{I-III} corresponding to $\lambda \rightarrow 1$. It is worth mentioning that autonomous limit of Eqs. (A1) could be written in the Suris form by introducing a new set of variables

$$X_n = e^{x_n/\epsilon}, \quad \alpha = e^{A/\epsilon}, \quad \beta = e^{B/\epsilon},$$

leading us to

$$\begin{aligned} dP_I^S : \quad x_{n+1} + x_{n-1} &= \epsilon \log \left[\frac{e^{x_n/\epsilon} + 1}{e^{\sigma x_n/\epsilon}} \right], \\ dP_{II}^S : \quad x_{n+1} + x_{n-1} &= A - \rho x_n, \end{aligned}$$

$$\begin{aligned} dP_{III}^S : \quad x_{n+1} + x_{n-1} &= \\ &= \epsilon \log \left[\frac{(e^{x_n/\epsilon} + e^{A/\epsilon})(e^{x_n/\epsilon} + e^{-A/\epsilon})}{(e^{x_n/\epsilon} + e^{B/\epsilon})(e^{x_n/\epsilon} + e^{-B/\epsilon})} \right]. \end{aligned} \quad (A2)$$

While the force function for dP_{II}^S is simply a linear function, two other cases are specific examples of integrable exponential Suris mapping.

The *ultradiscretized* form of Painlevé equations (udP) could be obtained by taking the limit $\epsilon \rightarrow 0$ in Eqs. (A2). At this point we should clarify the terminology: by saying “*discrete*” Painlevé equation we refer to the difference nature of the equation in contrast to nonlinear second-order ordinary differential Painlevé equations. The addition “*ultra*” refers to another level of discretization when the force function is transitioning from a smooth continuous to a piecewise linear function. Using identity

$$\lim_{\epsilon \rightarrow 0} \epsilon \log [\exp(x/\epsilon) + \exp(y/\epsilon)] = \max(x, y),$$

we arrive to

$$\begin{aligned} udP_I : \quad x_{n+1} + x_{n-1} &= \max(x_n, 0) - \sigma x_n, \\ udP_{II} : \quad x_{n+1} + x_{n-1} &= A - \rho x_n, \\ udP_{III} : \quad x_{n+1} + x_{n-1} &= \max(x_n, A) - \max(x_n, B) \\ &\quad + \max(x_n, -A) - \max(x_n, -B). \end{aligned} \quad (A3)$$

The udP equations (A3) have a symplectic Suris form $x_{n+1} + x_{n-1} = f(x_n)$ with following ultradiscrete piecewise linear

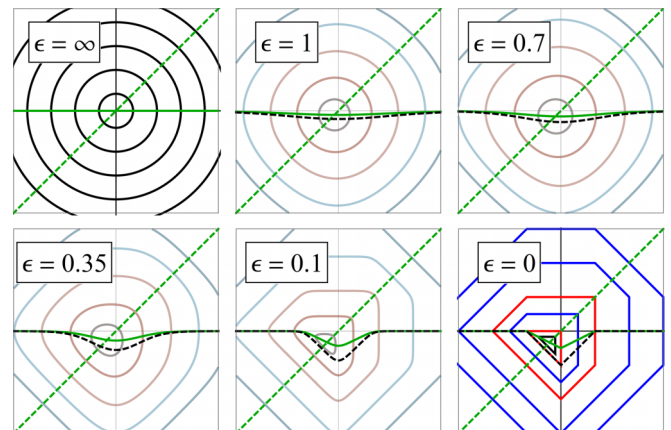


FIG. 18. Constant level sets of invariant on (x_n, x_{n+1}) plane for discrete Painlevé map dP_{III}^S in Suris form with $A = 0$ and x measured in units of B . For $\epsilon = \infty$ map degenerate to linear with $f(x) = 0$ and level sets degenerate to concentric circles. When $\epsilon = 0$ we observe ultradiscrete limit udP_{III} corresponding to polygon map $\alpha 3.1'$ with ratio of finite pieces restricted to unity, $r = 1$. Black and blue level sets show trajectories in linear and nonlinear areas of phase space, red level sets are separatrices of motion between different layers. Green curve is the second symmetry line $f(x)/2$ and black dashed curve is the force function $f(x)$.

force functions

$$\begin{aligned}
 f_I(x) &= \frac{|x| + x}{2} - \sigma x = \begin{cases} (1 - \sigma)x, & \text{for } x \geq 0, \\ -\sigma x, & \text{for } x < 0, \end{cases} \\
 f_{II}(x) &= A - \rho x, \\
 f_{III}(x) &= \frac{|x + A| + |x - A| - |x + B| - |x - B|}{2} \\
 &= \begin{cases} 0, & \text{for } x \in [B, \infty), \\ x - B, & \text{for } x \in [A, B), \\ A - B, & \text{for } x \in [-A, A), \\ -B - x, & \text{for } x \in [-B, -A), \\ 0, & \text{for } x \in (-\infty, -B). \end{cases} \quad (\text{A4})
 \end{aligned}$$

The force function f_I (corresponding to the first equation udP_I) is the simplest two-piece linear force without shift parameter, $d = 0$, and with slopes defined as $(k_1, k_2) = (-\sigma, 1 - \sigma)$. Since σ can only take values 0, 1, and 2, we obtain previously considered mappings G, F, and E, respectively (see Fig. 10). The second ultradiscretized Painlevé equation has a trivial linear force function f_{II} and is integrable for any values of parameters A and σ . In the case of integer slopes this results in three mappings with stable trajectories [26] α , β , γ and 2 unstable mappings a , b (see Fig. 10). Finally, for the third ultradiscretized Painlevé equation udP_{III} (assuming

$B > A > 0$), we obtain force function containing five pieces. Taking the limit $A = \text{const}$ and $B \rightarrow \infty$, from Eq. (A4) we have the linear map α with slope of force function $k_1 = -1$. Considering another limiting case $A \rightarrow 0$, one can see that $f(x)$ could be reduced to one of our four-piece polygon maps $\alpha 3.1'$ (slope coefficients $\{k_1, k_2, k_3, k_4\} = \{0, -1, 1, 0\}$ and $d = 2B$) with ratio parameter restricted to $r = 1$ (note that our map $\alpha 3.1'$ is integrable for arbitrary r). Figure 18 shows invariant level sets for this last case for different values of ϵ . As one can see, approaching the ultradiscrete level $\epsilon \rightarrow 0$, the force function transitions to piecewise linear and level sets transform to polygons. When $\epsilon = \infty$ map becomes linear with $v = 1/4$; note that invariant level sets are chosen as circles and not polygons. As we previously discussed linear mappings with rational rotation numbers are degenerate and allow infinitely many invariants of motion, but in this case the shape is chosen as a limiting case $\epsilon \rightarrow \infty$ for the exponential Suris invariant.

We emphasize that our polygon mappings represent a much richer family of integrable systems beyond ultradiscretizations of known Painlevé equations udP_{I-III} ; ultradiscretized equations of Painlevé type are limited to only five-piece force functions and the set of parameters is very restricted (e.g., slopes of outer pieces of five-piece force functions can only be equal to zero).

APPENDIX B: PSEUDOCODE FOR THE SEARCH ALGORITHM

Algorithm 1. Map analyzer. The algorithm verifies if a map is integrable with invariant level sets being polygons. The algorithm needs the function $\text{vertex}(q)$ and force function.

Input: $V^{\text{cutoff}} \in \mathbb{Z}$ —cutoff parameter for polygon vertex count,
 $q_{\text{ini}}^{\text{max}} \in \mathbb{Z}$ ($\sum_{i=2}^n l_i < q_{\text{ini}}^{\text{max}} < r_{\text{max}}$)—max initial condition.

Output: $\text{integrable} \in \mathbb{B}$ —integrability of map.

```

/* Map is integrable unless unstable or chaotic orbit is detected */ 
integrable ← True
/* Scan over all initial conditions from fixed point  $q^*$  to  $q_{\text{max}}$  */ 
for  $q = q^*, \dots, q_{\text{ini}}^{\text{max}}$  {
    /* Compute number of vertexes for given orbit */ 
     $V \leftarrow \text{vertex}(q)$ 
    /* If motion is stable */ 
    if  $V \neq -1$  then
        /* If the number of vertices in the orbit polygon is larger than a cutoff value,  $V^{\text{cutoff}}$  */ 
        if  $V > V^{\text{cutoff}}$  then
            /* Exclude map if any of orbits is chaotic */ 
            integrable ← False
        /* Exclude map if any of orbits is unstable */ 
        else integrable ← False
    }
    return integrable
  
```

Algorithm 2. Continuous piecewise linear force function $f(q, \mathbf{k}, \mathbf{l})$ with first vertex at the origin.

$$f(l_{s-1} < q \leq l_s, \mathbf{k}, \mathbf{l}) = k_s(q - \sum_{i=2}^{s-1} l_i) + \sum_{i=2}^{s-1} k_i l_i, \quad l_1 = 0, l_{0,n} = \mp\infty.$$

Input: $n \equiv \dim \mathbf{k} \geq 2$ —number of segments,

$q \in \mathbb{R}$ —coordinate,

$\mathbf{k} = (k_1, k_2, \dots, k_n) \in \mathbb{Z}^n$ — vector of slopes of segments,

$\mathbf{l} = (l_1, l_2, \dots, l_{n-1}) \in \mathbb{R}^{n-2}$ — vector of finite segments' length.

Output: $f(q, \mathbf{k}, \mathbf{l}) \in \mathbb{R}$ — value of force function.

```

/* Compute force function value depending on segment
switch q
{
    /* 1-st segment
    case q <= 0
        f ← k1q
    /* 2-nd segment
    case 0 < q <= l2
        f ← k2q
    /* 3-rd segment
    case l2 < q <= l2 + l3
        f ← k3(q - l2) + k2l2
    ...
    /* (n - 1)-th segment
    case ∑i=2n-2 li < q <= ∑i=2n-1 li
        f ← kn-1(q - ∑i=2n-2 li) + ∑i=2n-2 kili
    /* n-th segment
    case q > q ∑i=2n-1 li
        f ← kn(q - ∑i=2n-1 li) + ∑i=2n-1 kili
}
return f

```

APPENDIX C: MACHINE-DISCOVERED MAPPINGS WITH POLYGON INVARIANTS

The search results were classified as isolated, discrete and continuous with respect to parameters, when d and/or r is a finite set of integer values, take all integer values ($\in \mathbb{Z}$) or belongs to reals ($\in \mathbb{R}$), respectively. The results of the machine-assisted search for the three-piece force function are summarized in Fig. 19.

For force functions with four segments the results of a search are summarized in Tables II and III. In addition, more cases which were harder to classify are listed below. When $r = 1$, we found 2 dynamical systems which are integrable for any $d \in \mathbb{R}$: $\{0, -1, 0, -1\}$ and $\{1, 0, 1, 0\}$. In addition, map with slopes $\{-2, -1, -2, -1\}$ is integrable for any $d \geq 4$ (and its twin map $\{-1, -2, -1, -2\}$ is integrable for any $d \leq 3$). For values of r different from 1, the situation is getting more complicated and more families of mappings appear. For example, for previously semi-continuous map $\{-2, -1, -2, -1\}$, we have at least four

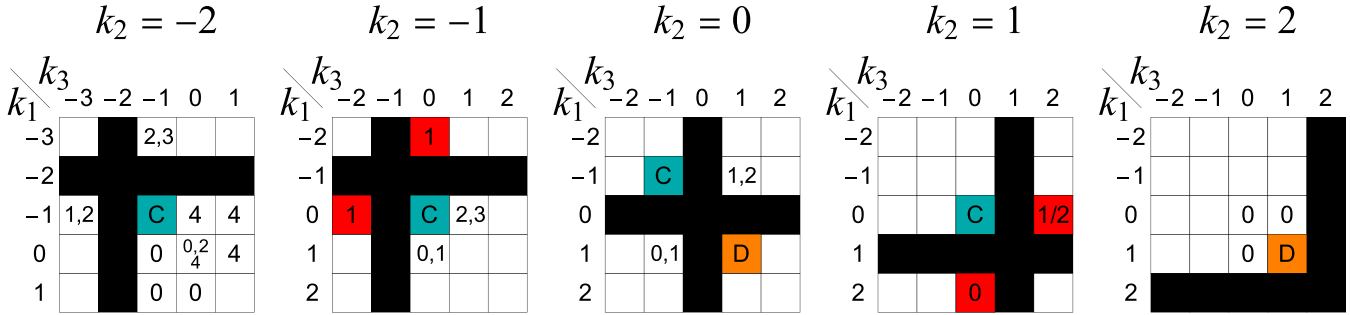


FIG. 19. Integrable polygon mappings corresponding to a piecewise linear force function with three segments. Each table corresponds to its own value of k_2 and shows the value of the shift parameter d . Black cells represent degenerate cases when three-piece force function becomes two-piece ($k_1 = k_2$ or $k_2 = k_3$), white cells represent cases with isolated integer d showing its values, orange cells represent mappings integrable for any integer $d \in \mathbb{Z}$ (“D”), cyan cells represent mappings integrable for continuous $d \in \mathbb{R}$ (“C”) and red cells represent unstable nonlinear polygon mappings where the numbers in the cell shows the values of d corresponding to integrable maps.

Algorithm 3. Function $vertex(q)$. The algorithm counts the number of vertexes V for a given orbit with initial condition on second symmetry line $(q, p) = (q_{\text{ini}}, f(q_{\text{ini}})/2)$ or returns value of (-1) if trajectory is unstable.

Input: $q_{\text{ini}} \in \mathbb{R}$ —initial coordinate on a second symmetry line,

$\mathbf{k} = (k_1, k_2, \dots, k_n) \in \mathbb{Z}^n$ — vector of slopes of segments,

$\mathbf{l} = (l_2, l_3, \dots, l_{n-1}) \in \mathbb{R}^{n-2}$ — vector of finite segments' length,

$d \in \mathbb{R}$ —force function shift parameter,

$N \in \mathbb{Z}$ —number of iterations,

$r_{\text{max}} \in \mathbb{R} (\gg \sum_{i=2}^{n-1} l_i)$ — max distance allowed in simulation,

$\eta \in \mathbb{R} \setminus \mathbb{Q} (\ll 1)$ —small irrational parameter to shift initial conditions,

$\epsilon \in \mathbb{R} (\ll 1)$ —collinearity cutoff parameter.

Output: V —number of vertex of orbit ($V = -1$ if orbit is unstable).

$V \leftarrow 0$

/* Initial condition on 2-nd symmetry line with small irrational shift */

$q \leftarrow q_{\text{ini}} + \eta$

$p \leftarrow [f(q, \mathbf{k}, \mathbf{l}) + d]/2$

/* Orbit, $\vec{\zeta} = (\zeta_1, \zeta_2, \dots, \zeta_N)$ */

for $i = 1, \dots, N$

{

$\zeta_i \leftarrow (q, p)$

$q' \leftarrow p$

$p' \leftarrow -q + f(p) + d$

$q \leftarrow q'$

$p \leftarrow p'$

/* Stop if radius of point in the phase space is $> r_{\text{max}}$ */

if $q^2 + p^2 > r_{\text{max}}^2$ then

{

$V \leftarrow -1$

break

}

else

{

/* Stop if orbit is periodic */

if $q' = q_{\text{ini}} \wedge p' = [f(q_{\text{ini}}, \mathbf{k}, \mathbf{l}) + d]/2$ then

break

}

}

/* Compute number of polygon vertexes, V , if the orbit is stable ($V \neq -1$) */

if $V \neq -1$ then

{

Sort $\vec{\zeta} = (\zeta_1, \dots, \zeta_N)$: $\forall 0 < k < N \quad [\arctan \frac{p_k}{q_k} > \arctan \frac{p_{k+1}}{q_{k+1}}]$

Add ζ_1 and ζ_2 to the tail of $\vec{\zeta}$: $\vec{\zeta} \leftarrow (\zeta_1, \zeta_2, \dots, \zeta_{N-1}, \zeta_N, \zeta_1, \zeta_2)$

for $j = 1, \dots, N$

{

/* Compute dot product between displacement vectors */

$\alpha_j = \frac{(p_{j+2} - p_{j+1})(p_{j+1} - p_j) + (q_{j+2} - q_{j+1})(q_{j+1} - q_j)}{\sqrt{(p_{j+2} - p_{j+1})^2 + (q_{j+2} - q_{j+1})^2} \sqrt{(p_{j+1} - p_j)^2 + (q_{j+1} - q_j)^2}}$

/* New polygon vertex detection */

if $||\alpha_j| - 1| > \epsilon$ then

$V++$

}

}

Return V

families with different behaviours of d :

$$\begin{aligned} d &= 4L_2 + 1 & (L_2 \geq 1), \\ d &= 4L_2 + 2 & (L_2 = 1, 2, 3, \dots), \\ d &= 4L_2 + 3 & (L_2 = 1, 3, 4, 6, 7, 9, 10, \dots), \\ d &= 5L_2 & (L_2 \geq 1); \end{aligned}$$

TABLE II. Integrable polygon mappings with four-piece force function and isolated integer d and r . Such mappings were found only for $r = 1, 2, 3$ and corresponding values of parameter d (in units of l_2) are presented for each quadruplet of integer slopes.

$[k_1, k_2, k_3, k_4]$	r			r			$[k_1, k_2, k_3, k_4]$
	1:1	1:2	1:3	1:3	1:2	1:1	
$[-1, -2, -1, -2]$		4,7					$[-2, -1, -2, -1]$
$[0, -2, 0, -1]$	2	0	2			4	$[-1, 0, -2, 0]$
$[0, -1, 1, -1]$	2			4		2	$[-1, 1, -1, 0]$
$[1, -2, 0, -1]$		0					$[-1, 0, -2, 1]$
$[1, -1, 0, -1]$	1		1			4	$[-1, 0, -1, 1]$
$[1, 0, 1, -1]$		1,2		4		2,1	$[-1, 1, 0, 1]$
$[1,0,2,0]$					0		$[0,2,0,1]$
$[1,2,0,1]$		0					$[1,0,2,1]$

we say at least because our algorithm was limited to the range of $r = [1, 2, \dots, 9, 10]$ and we cannot guarantee the absence of integrable mappings out of this range. Finally, three following groups of families were discovered

$\{0, -1, 0, -1\} :$

$$\begin{aligned} d &= L_2 & (L_2 \geq 0), \\ d &= L_2 + 1 & (L_2 \geq 0), \\ d &= 2L_2 + 1 & (L_2 \geq 0), \\ d &= 2L_2 + 2 & (L_2 = 1, 2, 3, \dots), \\ d &= 2L_2 + 3 & (L_2 = 1, 3, 4, 6, 7, 9, 10, \dots), \\ d &= 3L_2 & (L_2 \geq 1/2), \end{aligned}$$

$\{-1, 0, -1, 0\} :$

$$\begin{aligned} d &= 2L_2 & (L_2 \geq 0), \\ d &= 2L_2 + 1 & (L_2 \geq 0), \\ d &= 3L_2 + 1 & (L_2 \geq 0), \\ d &= 3L_2 + 2 & (L_2 = 1, 2, 3, \dots), \\ d &= 3L_2 + 3 & (L_2 = 1, 3, 4, 6, 7, 9, 10, \dots), \\ d &= 4L_2 & (L_2 \geq 1/2). \end{aligned}$$

$\{1, 0, 1, 0\} :$

$$\begin{aligned} d &= 0 & (L_2 \geq 0), \\ d &= 1 & (L_2 \geq 0), \\ d &= L_2 + 1 & (L_2 \geq 0), \\ d &= L_2 + 2 & (L_2 = 1, 2, 3, \dots), \\ d &= L_2 + 3 & (L_2 = 1, 3, 4, 6, 7, 9, 10, \dots), \\ d &= 2L_2 & (L_2 = 1/2 \text{ and } L_2 \geq 1), \\ d &= 2 & (L_1 : L_2 = 1 : 4), \end{aligned}$$

$\{0, 1, 0, 1\} :$

$$\begin{aligned} d &= L_2 & (L_2 \geq 0), \\ d &= L_2 + 1 & (L_2 \geq 0), \\ d &= 2L_2 + 1 & (L_2 \geq 0), \\ d &= 2L_2 + 2 & (L_2 = 1, 2, 3, \dots), \\ d &= 2L_2 + 3 & (L_2 = 1, 3, 4, 6, 7, 9, 10, \dots), \\ d &= 3L_2 & (L_2 = 1/2, 3/2 \text{ and } L_2 \geq 2). \end{aligned}$$

TABLE III. Integrable polygon mappings with four-piece force function and isolated integer d and discrete or continuous r . Values of parameters d (in units of l_2) and r are presented for each quadruplet of integer slopes.

$[k_1, k_2, k_3, k_4]$	d	r	r	d	$[k_1, k_2, k_3, k_4]$
$[0, -1, -2, -1]$	0	1	\mathbb{N}^+	$4 + 3/r$	$[-1, -2, -1, 0]$
	1	\mathbb{R}^+	\mathbb{R}^+	$4 + 2/r$	
$[0, -2, -1, 0]$	0	\mathbb{R}^+	\mathbb{R}^+	$3 + 4/r$	$[0, -1, -2, 0]$
	$2 + 1/r$	\mathbb{R}^+	\mathbb{R}^+	$2 + 2/r$	
	$4 + 2/r$	\mathbb{R}^+	\mathbb{R}^+	1	
$[0, -1, 1, 0]$	2	\mathbb{R}^+	\mathbb{R}^+	$1 + 1/r$	$[0, 1, -1, 0]$
$[0,1,2,0]$	1	\mathbb{R}^+	\mathbb{R}^+	0	$[0,2,1,0]$
$[1, -1, -2, -1]$	0	1	\mathbb{N}^+	$4 + 3/r$	$[-1, -2, -1, 1]$
$[1, -1, 0, -1]$	0	1	\mathbb{N}^+	$2 + 3/r$	$[-1, 0, -1, 1]$
$[1, 0, -2, -1]$			$2, 4, 6, \dots$	$4 + 3/(2r)$	$[-1, -2, 0, 1]$
$[1, -2, -1, 0]$	0	\mathbb{R}^+	\mathbb{R}^+	$3 + 4/r$	$[0, -1, -2, 1]$
$[1, 0, -1, 0]$	0	\mathbb{R}^+	\mathbb{R}^+	$3 + 2/r$	$[0, -1, 0, 1]$
	1	\mathbb{R}^+	\mathbb{R}^+	$3 + 1/r$	
	$1 + 1/r$	\mathbb{R}^+	\mathbb{R}^+	$2 + 1/r$	
$[1,2,1,0]$	0	\mathbb{R}^+	\mathbb{R}^+	1	$[0,1,2,1]$
	$1/r$	\mathbb{N}^+	1	0	

$$\begin{array}{lll}
 \{0, -1, 0, 1\} : & & \{1, 2, 1, 0\} : \\
 d = L_2 + 2 & (L_2 \geq 0), & d = 1 \quad (L_2 = 3, 4, 5, \dots), \\
 d = L_2 + 3 & (L_2 \geq 0), & d = (L_2/2) + 1 \quad (L_2 = 2, 6, 10, 14, \dots). \\
 d = 2L_2 + 1 & (L_2 = 1, 2, 4, 5, 7, 8, 10, \dots), & \\
 d = 2L_2 + 2 & (L_2 = 1, 2, 3, \dots), & \\
 d = 2L_2 + 3 & (L_2 \geq 0), & \\
 d = (3/2)L_2 + 7/2 & (L_2 = 1, 3, 5, 7, \dots), & \\
 d = (3/2)L_2 + 3 & (L_2 = 2, 4, 6, 8, \dots), & \\
 d = (5/3)L_2 + 10/3 & (L_2 = 1, 4, 7, 10, \dots), &
 \end{array}$$

[1] V. I. Arnold and A. Avez, *Ergodic Problems of Classical Mechanics*, Vol. 9 (Benjamin, Amsterdam, 1968).

[2] A. J. Lichtenberg and M. A. Lieberman, *Regular and Chaotic Dynamics*, Vol. 38 (Springer Science & Business Media, Berlin, 2013).

[3] J. D. Meiss, Symplectic maps, variational principles, and transport, *Rev. Mod. Phys.* **64**, 795 (1992).

[4] M. Šuvakov and V. Dmitrašinović, Three classes of Newtonian three-body planar periodic orbits, *Phys. Rev. Lett.* **110**, 114301 (2013).

[5] X. Li and S. Liao, More than six hundred new families of Newtonian periodic planar collisionless three-body orbits, *Sci. China Phys. Mech. Astron.* **60**, 129511 (2017).

[6] X. Li, Y. Jing, and S. Liao, Over a thousand new periodic orbits of a planar three-body system with unequal masses, *Publ. Astron. Soc. Jpn.* **70**, 64 (2018).

[7] R. Bondesan and A. Lamacraft, Learning symmetries of classical integrable systems, [arXiv:1906.04645](https://arxiv.org/abs/1906.04645).

[8] Z. Liu and M. Tegmark, Machine learning conservation laws from trajectories, *Phys. Rev. Lett.* **126**, 180604 (2021).

[9] S. Ha and H. Jeong, Discovering invariants via machine learning, *Phys. Rev. Res.* **3**, L042035 (2021).

[10] S. J. Wetzel, R. G. Melko, J. Scott, M. Panju, and V. Ganesh, Discovering symmetry invariants and conserved quantities by interpreting siamese neural networks, *Phys. Rev. Res.* **2**, 033499 (2020).

[11] D. Levi, L. Vinet, and P. Winternitz, *Symmetries and Integrability of Difference Equations* (Springer, Berlin, 1996).

[12] B. Grammaticos and A. Ramani, Discrete Painlevé equations: A review, *Discrete Integr. Syst.* **644**, 245 (2004).

[13] A. P. Veselov, Integrable maps, *Russian Math. Surveys* **46**, 1 (1991).

[14] E. M. McMillan, A problem in the stability of periodic systems, in *Topics in Modern Physics, a tribute to E. V. Condon*, edited by E. Brittin and H. Odabasi (Colorado Associated University Press, Boulder, CO, 1971), pp. 219–244.

[15] D. Turaev, Polynomial approximations of symplectic dynamics and richness of chaos in nonhyperbolic area-preserving maps, *Nonlinearity* **16**, 123 (2003).

[16] Y. B. Suris, Integrable mappings of the standard type, *Funct. Anal. Appl.* **23**, 74 (1989).

[17] M. Brown, The american mathematical monthly, *Am. Math. Mon.* **90**, 569 (1983).

[18] M. Brown and J. F. Slifker, The american mathematical monthly, *Am. Math. Mon.* **92**, 218 (1985).

[19] M. Brown, A periodic homeomorphism of the plane, *Continuum Theory and Dynamical Systems*, Lecture Notes in Pure and Appl. Math. 149 (Dekker, New York, 1993), pp. 83–87.

[20] B. V. Chirikov, Research concerning the theory of nonlinear resonance and stochasticity, Nuclear Physics Institute of the Siberian Section of the USSR academy of sciences, Report 267, Novosibirsk, 1969.

[21] B. V. Chirikov, A universal instability of many-dimensional oscillator systems, *Phys. Rep.* **52**, 263 (1979).

[22] M. Henon, Numerical study of quadratic area-preserving mappings, *Q. Appl. Math.* **27**, 291 (1969).

[23] D. C. Lewis Jr, Reversible transformations, *Pac. J. Math.* **11**, 1077 (1961).

[24] J. Bamberg, G. Cairns, and D. Kilminster, The crystallographic restriction, permutations, and Goldbach's conjecture, *Amer. Math. Monthly* **110**, 202 (2003).

[25] J. Kuzmanovich and A. Pavlichenkov, Finite groups of matrices whose entries are integers, *Amer. Math. Monthly* **109**, 173 (2002).

[26] G. Cairns, Y. Nikolayevsky, and G. Rossiter, Piecewise linear periodic maps of the plane with integer coefficients, [arXiv:1407.3364](https://arxiv.org/abs/1407.3364).

[27] G. Cairns, Y. Nikolayevsky, and G. Rossiter, Conewise linear periodic maps of the plane with integer coefficients, *Amer. Math. Monthly* **123**, 363 (2016).

[28] A. Beardon, S. Bullett, and P. Rippon, Periodic orbits of difference equations, *Proc. Roy. Soc. Edinburgh Sec. A: Math.* **125**, 657 (1995).

[29] J. C. Lagarias and E. Rains, Dynamics of a family of piecewise-linear area-preserving plane maps I. Rational rotation numbers, *J. Differ. Eq. Appl.* **11**, 1089 (2005).

[30] J. C. Lagarias and E. Rains, Dynamics of a family of piecewise-linear area-preserving plane maps II. Invariant circles, *J. Differ. Eq. Appl.* **11**, 1137 (2005).

[31] J. C. Lagarias and E. Rains, Dynamics of a family of piecewise-linear area-preserving plane maps III. Cantor set spectra, *J. Differ. Eq. Appl.* **11**, 1205 (2005).

[32] R. L. Devaney, A piecewise linear model for the zones of instability of an area-preserving map, *Physica D* **10**, 387 (1984).

[33] T. Zolkin and S. Nagaitev, Integrable and chaotic mappings of the plane with polygon invariants (2017), poster presented

at International ICFA mini-workshop Nonlinear Dynamics And Collective Effects In Particle Beam Physics (NOCE2017), Ar-cidosso, Italy, 19–22 September, 2017.

[34] T. Zolkin, S. Nagaitsev, and A. Halavanau, McMillan maps of polygon form, poster MOPGW108 presented at International Particle Accelerator Conference (IPAC19), Melbourne, Australia, 19–24 May, 2019.

[35] github.com/yourball/polygon-maps.

[36] J. Moser, Private communication, this is a conjecture of H. Cohen communicated by Y. Colin-de Verdiére to J. Moser, April 10, 1993.

[37] M. Rychlik and M. Torgerson, Algebraic nonintegrability of the Cohen map, *New York J. Math.* **4**, 74 (1998).

[38] C. Skokos, C. Antonopoulos, T. Bountis, and M. Vrahatis, Smaller alignment index (SALI): Determining the ordered or chaotic nature of orbits in conservative dynamical systems, in *Libration Point Orbits And Applications* (World Scientific, Singapore, 2003), pp. 653–664.

[39] S. Antipov, D. Broemmelsiek, D. Bruhwiler, D. Edstrom, E. Harms, V. Lebedev, J. Leibfritz, S. Nagaitsev, C. Park, H. Piekarz, P. Piot, E. Prebys, A. Romanov, J. Ruan, T. Sen, G. Stancari, C. Thangaraj, R. Thurman-Keup, A. Valishev, and V. Shiltsev, IOTA (integrable optics test accelerator): Facility and experimental beam physics program, *J. Instrum.* **12** (03), T03002 (2017).